

Model for pedestal structure

J.D. Callen^{1, a)}

University of Wisconsin, Madison, WI 53706-1609

(Dated: 7 November 2011)

Predictions are developed for the structure of plasma parameter profiles of high-confinement (H)-mode pedestals in transport quasi-equilibrium in tokamaks. They are based on assuming paleoclassical radial plasma transport processes dominate throughout the pedestal. The key physical process in this model is that the electron temperature gradient increases to the magnitude required for paleoclassical electron heat transport to carry the large conductive radial electron heat flow from the hot core through the pedestal to the separatrix. The intrinsic level of paleoclassical density transport is typically large in the pedestal compared to local fueling due to neutral recycling from outside the separatrix. Thus, in this model the electron density profile is determined mainly not by edge fueling but rather by a combination of the density boundary condition at the separatrix and the pedestal density profile needed for the outward paleoclassical diffusive flux to be nearly balanced by the inward paleoclassical pinch flux. Model predictions are given for the electron density and temperature gradients, profiles and magnitudes in the pedestal. Transition into electron-temperature-gradient (ETG) driven anomalous radial electron heat transport in the core plasma is proposed to limit the initial, transport-limited height of the electron pressure pedestal. Characteristics of the ion temperature and plasma toroidal rotation profiles in the pedestal are also predicted. All the model predictions are found to agree quantitatively (within a factor of about two or less) with the properties of an extensively studied H-mode pedestal. Other model comparisons and applications to some outstanding H-mode pedestal structure and evolution issues in tokamaks are also discussed. Finally, a hierarchy of experimental and modeling validation tests are suggested.

PACS numbers: 52.55.Fa, 52.25.Fi, 52.55.Dy, 52.25.Xz, 52.55.Rk

I. INTRODUCTION

A recent study¹ of plasma transport properties in a carefully diagnosed and analyzed single DIII-D² high-confinement (H)-mode pedestal indicated it is quite plausible that paleoclassical plasma transport^{3,4} is a significant contributor in this pedestal. Specifically, pedestal electron heat and density transport (diffusivities plus density pinch) were found¹ to be in reasonable agreement with paleoclassical predictions. Also, the magnitudes and profiles of the electron heat diffusivity, and density profiles in the pedestal have been found to approximately agree with paleoclassical-based model predictions in the National Spherical Tokamak Experiment (NSTX) pedestals⁵ for discharges both without and with lithium-coated plasma-facing components.

This paper develops a comprehensive set of paleoclassical model predictions for plasma profiles in H-mode pedestals that are in transport “quasi-equilibrium.” The steady-state “pedestal structure” will be determined for pedestals that have properties similar to those in the DIII-D 98889 pedestal,¹ whose edge profiles are shown in Fig. 1. This will often be referred to henceforth as the “98889 pedestal.” The fundamentals and two key predictions of the model are being published elsewhere⁶ and were used in Ref. 5. The more comprehensive set of predictions developed here are compared quantitatively with data from the 98889 pedestal.¹ They are also used

to interpret a number of properties in similar H-mode pedestals in DIII-D and other tokamaks, and evolution toward Edge Localized Modes (ELMs) in them. Three sets of experimental and modeling validation tests for this new pedestal structure model are also proposed.

The fundamental physics of the model developed here can be understood as follows. First, one notes that often most of the heat flowing through pedestals is carried by electrons — about 75% in the 98889 pedestal.¹ Because most plasma heating occurs in the hotter and denser core, a large electron heat flux must be carried out through the lower density and temperature pedestal. Thus, from a Fourier heat flux law $\mathbf{q}_e = -n_e\chi_e\nabla T_e$, the electron temperature gradient in the pedestal will increase until this large heat flux can be carried out through the pedestal to the separatrix. The needed electron temperature gradient ($\mathbf{q}_e/n_e\chi_e$) is determined by the effective electron heat diffusivity χ_e in the pedestal.

The key assumption in this paper is that paleoclassical processes dominate χ_e and all plasma transport channels (except for ion heat transport which may have a significant neoclassical component) in the steep gradient region of the pedestal. As discussed after Eq. (26) below, the inherent level of paleoclassical density transport is usually large in the pedestal compared to the typically small local fueling from edge neutral recycling. Thus, in this model the n_e profile in the pedestal is usually determined not by local fueling but rather by what it needs to be for the paleoclassical density transport operator to be small. That is, the density profile will be that which causes the outward paleoclassical diffusive density flux to be nearly

^{a)}callen@engr.wisc.edu; <http://www.cae.wisc.edu/~callen>

balanced by the inward paleoclassical pinch flux. This inward pinch flux is an intrinsic model characteristic that results naturally from the unique structure of the paleoclassical density transport operator.

Anomalous plasma transport due to microturbulence is usually dominant in the hotter, denser core in region I of Fig. 1. The abrupt change in the gradients of n_e and T_e from region I to II in Fig. 1 is likely due to a change from core anomalous transport to another dominant transport mechanism in the pedestal (II, III) — here postulated to be paleoclassical transport. While fluctuations are usually present in pedestals and likely peak where the plasma pressure gradient is largest (near the II→III transition), they will be assumed to be too small to cause the dominant plasma transport within the pedestal. Anomalous transport fluxes will be allowed for in the development of general plasma transport and flow equations. However, anomalous transport effects will be explicitly dropped in determining the structure of plasma profiles within the pedestal; the anomalous fluxes will be re-introduced to provide estimates of their possible effects on the density gradient in the pedestal and the initial, transport-limited pedestal height from the region II→I transition. The possibly complementary role of Kinetic Ballooning Modes (KBMs) in limiting the maximum pressure gradient in the pedestal is discussed in Section X.

This paper is organized as follows. The next section describes relevant properties of the DIII-D 98889 pedestal¹ to which many model predictions will be compared. The following two sections (III and IV) present formulas for key paleoclassical transport model parameters and the simplified plasma transport equations that will be used here. The following sections (V–VIII) develop predictions for key properties of electron density, electron temperature, ion temperature and toroidal plasma flow profiles in the pedestal. Dimensionless variable scalings of the predictions are discussed in Section IX. The following section discusses some key issues for and other applications of this model. The penultimate section (XI) suggests a hierarchy of experimental and modeling validation tests for this new pedestal structure model. The final section summarizes the main pedestal structure predictions developed in this paper and their implications.

II. H-MODE PEDESTAL PROPERTIES

Many pedestal structure model predictions will be compared to plasma transport quasi-equilibrium profiles in the edge of the low collisionality DIII-D tokamak discharge 98889¹ shown in Fig. 1. The radial coordinate $\rho_N \equiv \rho/a$ is the normalized minor radius in terms of the toroidal-flux-based radial coordinate $\rho \equiv \sqrt{\psi_t/\pi B_t}$ (m).

The key edge plasma regions here are: core (I, $\rho_N < 0.96$), steep gradient region of the pedestal (II and III, $0.96 < \rho_N < 1$) and scrape-off-layer outside the magnetic separatrix at $\rho_N = 1$ ($a \simeq 0.77$ m) in this lower single null diverted plasma. The pedestal top will be identified here

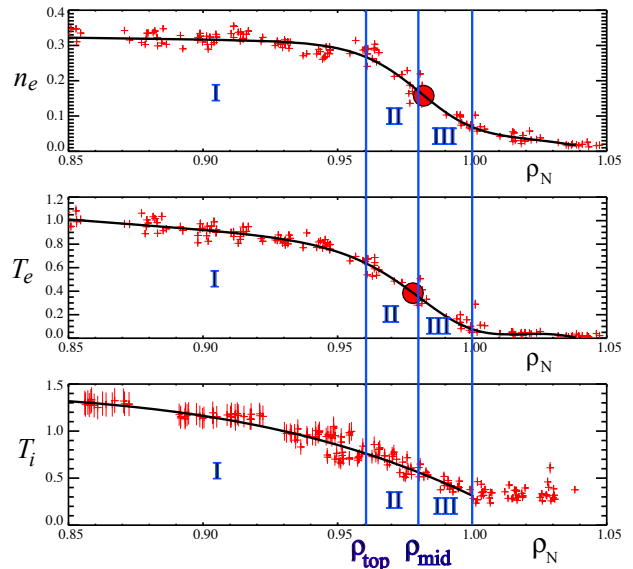


FIG. 1. Electron density n_e ($\times 10^{20} \text{ m}^{-3}$) and temperature T_e (keV), and ion temperature T_i (keV) profiles in the edge of DIII-D discharge 98889.¹ The large red dots indicate where the maximum gradients occur.

TABLE I. Key parameters for the DIII-D 98889 pedestal.¹

Parameter	at ρ_{top}	at ρ_{mid}	at $\rho_{\text{sep}} = a$
T_e (eV)	666	352	89
$n_e/10^{19} \text{ m}^{-3}$	2.76	1.77	0.77
Z_{eff}	2.83	2.6	1.9
$\epsilon \equiv r_M/R_0$	0.347	0.352	0.356
f_t/f_c	3.24	3.31	3.38
$\ln \Lambda$	16.0	15.5	14.6
$\nu_e(\text{s}^{-1})/10^5$	2.1	3.15	7.4
λ_e (m)	73	35	7.6
$\nu_e/\omega_{te} \equiv R_0 q/\lambda_e$	0.10	0.21	∞
$M \simeq \lambda_e/(\pi R_0 q)$	3.1	1.5	0.0
Usual $\nu_e/\epsilon^{3/2}\omega_{te}$	0.5	1.0	∞
ν_{*e} defined here	1.9	3.9	∞
μ_e/ν_e	0.57	0.30	0.0
$\eta_{\parallel}^{\text{sp}}/\eta_0$	0.40	0.41	0.44
$\eta_{\parallel}^{\text{nc}}/\eta_0$	0.81	0.69	0.44
Eq. (9) / D_η	1.19	1.03	1.0
$D_\eta \equiv \eta_{\parallel}^{\text{nc}}/\mu_0$ ($\text{m}^2 \text{ s}^{-1}$)	0.175	0.345	1.2

as being at $\rho_{\text{top}} = 0.96 a$. The pedestal mid-point at $\rho_{\text{mid}} = 0.98 a$ is indicated by the middle blue vertical line between regions II and III in Fig. 1. The profile fitting procedures and characteristics are discussed in Ref. 1.

Table I provides values of relevant parameters for the data shown in Fig. 1 for which the mid-plane half-width $r_M(\rho_{\text{mid}}) \simeq 0.6$ m, major radius $R_0 \simeq 1.7$ m, and “safety factor” $q(\rho_{\text{mid}}) \simeq 4.5$. On the separatrix $q \rightarrow \infty$. The remaining parameters in Table I will be defined and discussed in the next section.

III. KEY ELEMENTS OF PALEOCLASSICAL THEORY

The initial paleoclassical papers^{3,4,7} were based on a key hypothesis that charged particles diffuse radially along with thin annuli of poloidal magnetic flux in resistive, current-carrying toroidal plasmas. That is, they diffuse radially with the magnetic field diffusivity $D_\eta = \eta/\mu_0$, in which η is the plasma electrical resistivity. This hypothesis was later shown⁸ to result from transforming the drift-kinetic equation from laboratory to poloidal magnetic flux coordinates, upon which Grad-Shafranov magnetohydrodynamic (MHD) equilibria, neoclassical transport theory and gyrokinetic-based microturbulence-induced anomalous transport analyses are all based. This derivation was critiqued in Comments in Refs. 9, 11 and corresponding Responses provided in Refs. 10, 12. In particular, Ref. 11 asserted the “mathematical manipulations ... appear to lack a systematic basis.” The Response¹² provided a systematic multiple-time-scale analysis of electron guiding center motion that reproduced the results in Ref. 8. The paleoclassical key hypothesis has now been derived three different ways: by integrating along characteristics of the drift kinetic equation,⁸ using a phenomenological approach¹⁰ and from a systematic multiple-time-scale analysis.¹²

The diffusive components of paleoclassical plasma transport are proportional to the plasma resistivity η whose Spitzer form scales as $T_e^{-3/2}$. The lower limit paleoclassical radial electron heat transport ($\chi_e^{\text{pc}} \propto a^{1/2} T_e^{-3/2}$) can be greater than fluctuation-induced gyroBohm-level transport ($\chi_e^{\text{gB}} \propto T_e^{3/2}/aB^2$) wherever¹³ $T_e < B(\text{T})^{2/3} a(\text{m})^{1/2}$ keV, which usually occurs in ohmic tokamak plasmas, or wherever fluctuations are significantly reduced. Thus, paleoclassical electron heat transport is likely to be dominant in H-mode pedestals¹³ — for $T_e \lesssim 1$ keV in DIII-D and $T_e \lesssim 5$ keV in ITER.¹⁴ In (low) L-mode plasmas the fluctuation-induced transport usually exceeds the irreducible minimum paleoclassical plasma transport, particularly in the edge. However, paleoclassical transport predictions compare favorably with experimental data from many ohmic-level toroidal plasmas¹³ (tokamaks, spherical tokamaks, reversed field pinches, spheromaks), in electron-cyclotron (EC) heated plasmas in RTP¹⁵ and in tokamak H-mode pedestals.^{1,13}

The fundamental parameter of the paleoclassical transport model is the diffusivity coefficient ($\text{m}^2 \text{s}^{-1}$) for poloidal magnetic flux diffusion^{4,7,16,17}

$$D_\eta \equiv \frac{\eta_{\parallel}^{\text{nc}}}{\mu_0} = \frac{\eta_0}{\mu_0} \frac{\eta_{\parallel}^{\text{nc}}}{\eta_0}, \quad \text{magnetic field diffusivity.} \quad (1)$$

Since $\mu_0 \equiv 4\pi \times 10^{-7} \text{ N A}^{-2}$ (in SI, MKS units) is a constant of nature, the key parameter is really the parallel neoclassical resistivity $\eta_{\parallel}^{\text{nc}}$. The reference, perpendicular resistivity $\eta_0 \equiv m_e \nu_e / n_e e^2$ can be written in the form of

a magnetic field diffusivity as

$$\frac{\eta_0}{\mu_0} \equiv \frac{m_e \nu_e}{\mu_0 n_e e^2} \simeq \frac{1400 Z}{[T_e(\text{eV})]^{3/2}} \left(\frac{\ln \Lambda}{17} \right), \quad \frac{\text{m}^2}{\text{s}}. \quad (2)$$

Here and below, $Z \rightarrow Z_{\text{eff}} \equiv \sum_i n_i Z_i^2 / n_e$ is the effective ion charge and $\ln \Lambda$ is the Coulomb logarithm.

The parallel neoclassical resistivity $\eta_{\parallel}^{\text{nc}}$ (Ohm-m) can be evaluated using one of formulas in the literature;^{18–22} the NCLASS²³ code is often used to evaluate it. In this paper $\eta_{\parallel}^{\text{nc}}$ is evaluated by inverting the 2×2 matrix of the friction and viscosity coefficient matrices in the combination of electron parallel flow and heat flow equations that result from the moment approach to neoclassical plasma transport theory.^{20,22,24} The *Mathematica*[®] notebook file used to calculate $\eta_{\parallel}^{\text{nc}}$ and D_η values used in this paper is provided as supplementary material.²⁵ The parallel neoclassical resistivity values used here are within 20% of the values obtained from the various formulas in the literature,^{6,18–21} which deviate similarly from each other for pedestal region parameters.

A useful and physically illustrative approximate formula for the ratio of neoclassical resistivity to η_0 is^{4,7}

$$\frac{\eta_{\parallel}^{\text{nc}}}{\eta_0} \simeq \frac{\eta_{\parallel}^{\text{Sp}}}{\eta_0} + \frac{\mu_e}{\nu_e}, \quad \text{neoclassical resistivity factor.} \quad (3)$$

The two components of the parallel resistivity are^{4,6,7}

$$\begin{aligned} \frac{\eta_{\parallel}^{\text{Sp}}}{\eta_0} &\simeq \frac{\sqrt{2} + Z}{\sqrt{2} + 13Z/4}, \quad \text{Spitzer factor, and} \quad (4) \\ \frac{\mu_e}{\nu_e} &\simeq \frac{(f_t/f_c)(1 + 0.533/Z)}{[1 + \nu_{*e}^{1/2} + 1.65(1 + 0.533/Z)\nu_{*e}][1 + \nu_e/\omega_{te}]}, \quad (5) \end{aligned}$$

which represents effects of the electron viscous damping with frequency μ_e . Here, f_c is the flow-weighted fraction of circulating particles²⁰ with Padé approximate²⁶

$$\begin{aligned} f_c &\equiv \frac{3}{4} \langle B^2 \rangle \int_0^{B_{\text{max}}} \frac{\lambda d\lambda}{\langle \sqrt{1 - \lambda B(\theta)} \rangle} \\ &\simeq \frac{(1 - \epsilon^2)^{-1/2} (1 - \epsilon)^2}{1 + 1.46 \epsilon^{1/2} + 0.2 \epsilon} \quad \epsilon \lesssim 1 \quad 1 - 1.46 \epsilon^{1/2}, \quad (6) \end{aligned}$$

in which the $\langle \dots \rangle$ indicates the flux surface average and $\epsilon \equiv (B_{\text{max}} - B_{\text{min}})/(B_{\text{max}} + B_{\text{min}}) \simeq r_M/R_0$ is the local magnetic inverse aspect ratio. The fraction of trapped particles is $f_t \equiv 1 - f_c$. Other approximate formulas for f_c have also been presented in the literature.^{24,27} For 98889 pedestal parameters in Table I $\epsilon \simeq 0.35$ and $f_t/f_c \simeq 0.77/0.23 \simeq 3.3 \gg 1$. For the highly noncircular near-separatrix geometry in DIII-D, f_c should really be evaluated numerically^{20,21} using the first form in (6).

The neoclassical electron collisionality parameter for the large f_t/f_c values in H-mode pedestals is^{20,22,24}

$$\begin{aligned} \nu_{*e} &\equiv \frac{(f_t/f_c) \nu_e}{2.92 \nu_{T_e}} \frac{\langle B^2 \rangle / R_0 q}{\langle (\hat{\mathbf{b}} \cdot \nabla B)^2 \rangle} \simeq \frac{f_t/f_c}{1.46 \epsilon^2} \frac{\nu_e}{\omega_{te}} \\ &= \frac{f_t/f_c}{1.46 \epsilon^2} \frac{R_0 q}{\lambda_e} \frac{\epsilon \lesssim 1}{\epsilon^{3/2} \omega_{te}}. \quad (7) \end{aligned}$$

Here, the electron thermal speed $v_{T_e} \equiv \sqrt{2T_e/m_e}$, the electron “transit” frequency $\omega_{te} \equiv v_{T_e}/R_0q$, and for the first approximate equality $\langle (\mathbf{b} \cdot \nabla B)^2 \rangle / \langle B^2 \rangle \simeq \epsilon^2 / 2R_0^2 q^2$ has been used. This ν_{*e} is $\sqrt{2}$ smaller than that defined in Refs. 18, 21 in the $\epsilon \ll 1$ limit. Also, the electron Coulomb collision length (“mean free path”) is

$$\lambda_e \equiv \frac{v_{T_e}}{\nu_e} \simeq 1.2 \times 10^{16} \frac{[T_e(\text{eV})]^2}{Z n_e(\text{m}^{-3})} \left(\frac{17}{\ln \Lambda} \right) \text{ m}. \quad (8)$$

Because the fraction of trapped particles f_t is large in most tokamak H-mode pedestals, the relevant electron collisionality parameter ν_{*e} is larger than the usual¹⁸ $\nu_e/\epsilon^{3/2}\omega_{te}$ formula by a factor of $(f_t/f_c)/(1.46\epsilon^{1/2})$. For example, $\nu_{*e}(\rho_{\text{mid}}) \simeq 3.9$ is about a factor of 4 larger than the usual small ϵ formula result which yields 1.0 at ρ_{mid} in the 98889 pedestal.¹ Thus, as indicated in Table I, because of their low aspect ratio ($1/\epsilon \sim 2.8$ in DIII-D), pedestal plasmas are usually not in the low collisionality ($\nu_{*e} \ll 1$) “banana” regime; rather, they are usually in the intermediate collisionality “plateau” or even Pfirsch-Schlüter ($\nu_e > \omega_{te}$) regimes.^{18,20}

An approximate formula for D_η for typical H-mode pedestals where $Z_{\text{eff}} \simeq 1.9$ –2.8 so that $1+0.533/Z_{\text{eff}} \simeq 1.2$ can be written using $\ln \Lambda \simeq 15.8$ as⁶

$$D_\eta \simeq \frac{1300 Z_{\text{eff}}}{[T_e(\text{eV})]^{3/2}} \left(0.41 + \frac{1.2(f_t/f_c)/(1+\nu_e/\omega_{te})}{1+\nu_{*e}^{1/2}+2\nu_{*e}} \right) \frac{\text{m}^2}{\text{s}}. \quad (9)$$

A slight variant of this approximate formula for D_η with $1.2 \rightarrow 1+0.533/Z_{\text{eff}}$ was used in previous comparisons of the basic pedestal model predictions with data from NSTX⁵ and DIII-D.⁶ As indicated in the next to last line in Table I, the approximation to D_η in (9) yields values that are within 20% of the values obtained from the more precise 2×2 matrix inversion results used throughout this paper. This causes the comparisons with data from the 98889 pedestal to similarly deviate slightly from the corresponding estimates in Ref. 6.

As indicated in Table I, the $\eta_{\parallel}^{\text{nc}}/\eta_0$ factor in (1) increases by a factor of about two in moving from the separatrix to the top of the pedestal. Thus, while $Z_{\text{eff}}/T_e^{3/2}$ decreases by a factor of $(1.9/2.83)(666/89)^{3/2} \simeq 14$ from the separatrix to the top of the pedestal, $\eta_{\parallel}^{\text{nc}}$ and D_η only decrease by a factor of about 7. That is, while the dominant scaling is $D_\eta \sim Z_{\text{eff}}/T_e^{3/2}$, the μ_e electron viscosity effects are significant and cause the D_η scaling to be more complicated. Hence, the Z_{eff} and finite ϵ , ν_{*e} effects in (1)–(8) are important in determining the magnitude and scaling of D_η in H-mode pedestals.

While most paleoclassical transport processes are governed by D_η , paleoclassical electron heat transport includes an extra factor M .⁴ This factor arises from the addition of helically-resonant radial electron heat transport contributions⁴ in the vicinity of medium order rational surfaces. The multiplier M can be written as a smoothed (Padé approximate) formula^{4,7,13} $M \simeq [1/(\pi R_0 q)]/[1/\ell_{\text{max}} + 1/\lambda_e]$. It is determined

by the minimum of the collision length λ_e defined in (8) and an electromagnetic-skin-depth-determined parallel length ℓ_{max} over which thin annuli of poloidal flux diffuse radially.⁴ Throughout the 98889 pedestal $\lambda_e < \ell_{\text{max}}$ so $M \simeq \lambda_e/(\pi R_0 q)$. As indicated in Table I, for this approximation M decreases from about 3.1 at ρ_{top} , to 1.5 at ρ_{mid} , to zero at ρ_{sep} (where $q \rightarrow \infty$).

IV. PLASMA TRANSPORT EQUATIONS

In plasma transport quasi-equilibrium states shortly after ($\gtrsim 10$ ms) an L-H transition or just before an edge-localized-mode (ELM) such as those discussed in Refs. 1, 28, the “steady-state” ($\partial/\partial t \rightarrow 0$) flux-surface-averaged (FSA) plasma transport equations¹⁷ can be written as

$$\langle \nabla \cdot \mathbf{\Gamma} \rangle \equiv \frac{1}{V'} \frac{d}{d\rho} (V' \Gamma) = \langle S_n \rangle, \text{ density}, \quad (10)$$

$$\langle \nabla \cdot \mathbf{q}^{\text{pc}} \rangle + \frac{1}{V'} \frac{d}{d\rho} [V' (\Upsilon + \frac{5}{2} T \Gamma)] = Q^{\text{net}}, \text{ energy}. \quad (11)$$

Here: $\mathbf{\Gamma}$, \mathbf{q} are the density, heat fluxes; $\Gamma \equiv \langle \mathbf{\Gamma} \cdot \nabla \rho \rangle$, $\Upsilon \equiv \langle \mathbf{q} \cdot \nabla \rho \rangle$ are the corresponding FSA fluxes; $\langle \nabla \cdot \mathbf{q}^{\text{pc}} \rangle$ is the paleoclassical heat transport operator specified in Eq. (18) below; and $\langle S_n \rangle$, Q^{net} are the net FSA density, energy sources. In these equations ρ is the radial coordinate, which has units of m, and $V' \equiv dV/d\rho$ (m^2) is the radial derivative of the volume $V(\rho)$ (m^3) of the ρ flux surface. In the 98889 pedestal¹ $V' \simeq 43.4 \rho_N \text{ m}^2$.

The density equation will be considered first. The paleoclassical density transport operator can be written^{16,17} in the standard divergence form of an ambipolar paleoclassical density flux Γ^{pc} ($\text{m}^{-2} \text{ s}^{-1}$):

$$\Gamma^{\text{pc}} = - \frac{1}{V'} \frac{d}{d\rho} (V' \bar{D}_\eta n) = - \bar{D}_\eta \frac{dn}{d\rho} + n V_{\text{pinch}}. \quad (12)$$

As indicated, unlike the the usual Fick’s diffusion law form, Γ^{pc} naturally includes both diffusive and pinch fluxes. The pinch flux results from particle guiding centers only diffusing radially because the $\mathcal{O}\{\epsilon^2\}$ drag-type term in the Fokker-Planck paleoclassical transport operator is negligible.^{4,8} The usually inward (< 0) pinch velocity is

$$V_{\text{pinch}} \equiv - \frac{1}{V'} \frac{d}{d\rho} (V' \bar{D}_\eta), \quad \text{pinch flow, m s}^{-1}. \quad (13)$$

Here, the geometrically-effective flux-surface-averaged magnetic field diffusivity \bar{D}_η ($\text{m}^2 \text{ s}^{-1}$), which is the key parameter in all paleoclassical contributions to the plasma transport equations and results throughout the remainder of this paper, is⁴

$$\bar{D}_\eta \equiv \frac{a^2}{\bar{a}^2} D_\eta, \quad \text{in which } \frac{a^2}{\bar{a}^2} \equiv \left\langle \frac{|\nabla \rho|^2}{R^2 (R^{-2})} \right\rangle. \quad (14)$$

The a^2/\bar{a}^2 factor is slightly smaller than the usual $\langle |\nabla\rho|^2 \rangle$ geometric factor that arises from using standard Fick's or Fourier's law diffusive fluxes, which was important in the Ref. 1 transport analysis. In the 98889 pedestal $a^2/\bar{a}^2 \simeq 1.6$ so in these pedestals $\bar{D}_\eta \simeq 1.6 D_\eta$. Figure 7 in Ref. 1 indicates that $\langle |\nabla\rho|^2 \rangle \simeq 2$ in the 98889 pedestal. Both of these geometric quantities diverge weakly as $\ln q$ at the separatrix where $q \rightarrow \infty$.

Any additional density flux Γ^{add} induced by collisions or microturbulence will be left general for now. Adding paleoclassical and possible additional density transport fluxes Γ^{add} , the density (continuity) equation becomes

$$\frac{1}{V'} \frac{d}{d\rho} \left(-\frac{d}{d\rho} (V' \bar{D}_\eta n) + V' \Gamma^{\text{add}} \right) = \langle S_n \rangle. \quad (15)$$

Multiplying this equation by the differential volume $dV \equiv V' d\rho$ and integrating radially from the ρ flux surface to the separatrix ($\rho_{\text{sep}} \equiv a$) yields the equation that will be analyzed in the next section to determine properties of the pedestal density profile:

$$-\left[\frac{d}{d\rho} (V' \bar{D}_\eta n) \right]_\rho = \dot{N}(\rho) - [V' \Gamma^{\text{add}}]_\rho. \quad (16)$$

Here, $\dot{N}(\rho)$ is the number of charged particles per second (s^{-1}) that cross the ρ flux surface:

$$\dot{N}(\rho) \equiv \dot{N}(a) - \Delta \dot{N}(\rho), \quad (17)$$

whose two terms represent the number of charged particles per second crossing the separatrix $\dot{N}(a) = -(d/d\rho)[V' \bar{D}_\eta n]_a + [V' \Gamma^{\text{add}}]_a$ minus an integral correction $\Delta \dot{N}(\rho) \equiv \int_\rho^a d\hat{\rho} V'(\hat{\rho}) \langle S_n(\hat{\rho}) \rangle$ due to the local density source $\langle S_n \rangle$ between the ρ flux surface and the separatrix. And in (16) the term $[V' \Gamma^{\text{add}}]_\rho$ represents any additional charged particle losses across the ρ surface due to Γ^{add} .

Since the dominant radial heat flow through the pedestal is often via electrons, the electron energy balance will be discussed next. The FSA paleoclassical radial electron heat transport operator is not in the standard form of the divergence of a radial electron heat flux. Rather, it has a multiplier $M+1$ times a divergence.⁴ The paleoclassical electron heat transport operator is (see Eq. (142) in Ref. 4 or the sum of Eqs. (47) and (72) in Ref. 17)

$$\langle \nabla \cdot \mathbf{q}_e^{\text{pc}} \rangle = -\frac{M+1}{V'} \frac{d^2}{d\rho^2} \left(V' \bar{D}_\eta \frac{3}{2} n_e T_e \right), \quad \frac{W}{m^3}. \quad (18)$$

While the paleoclassical electron heat transport operator is non-standard, it often yields dominantly diffusive radial electron heat transport with an effective $\chi_e^{\text{pc}} \simeq (3/2)(M+1)D_\eta$ in the core of a tokamak plasma.^{4,7,13}

Possible additional electron heat fluxes Υ_e^{add} induced by collisions and microturbulence will be left general for now. Adding paleoclassical and possible additional electron heat fluxes, the electron energy equation becomes

$$-\frac{M+1}{V'} \frac{d^2}{d\rho^2} \left(V' \bar{D}_\eta \frac{3}{2} n_e T_e \right) + \frac{1}{V'} \frac{d}{d\rho} \left[V' \left(\Upsilon_e^{\text{add}} + \frac{5}{2} T_e \Gamma \right) \right] = Q_e^{\text{net}}. \quad (19)$$

Here, $\Gamma \equiv \Gamma^{\text{pc}} + \Gamma^{\text{add}}$ is the total (ambipolar) FSA density flux and Q_e^{net} is the net local electron heating rate which includes ohmic and neutral beam heating, ion-electron collisional energy exchange, radiation, etc. Multiplying this last equation by $V'/(M+1)$ and then integrating radially from a given ρ surface outward to the separatrix at a yields the equation for electron heat flow (W) that will be analyzed in Section VI to determine properties of the T_e profile:

$$-\left[\frac{d}{d\rho} \left(V' \bar{D}_\eta \frac{3}{2} n_e T_e \right) \right]_\rho = P_e(\rho) + \int_\rho^a \frac{d\hat{\rho}}{M(\hat{\rho})+1} \frac{d}{d\hat{\rho}} [V'(\hat{\rho}) \Upsilon_e^{\text{add}}(\hat{\rho})]. \quad (20)$$

Here, $P_e(\rho)$ is the effective conductive electron heat flow (W) through the ρ flux surface defined by

$$P_e(\rho) \equiv P_e(a) - \Delta P_e(\rho), \quad (21)$$

in which $P_e(a) = -[(d/d\rho)(V' \bar{D}_\eta (3/2)n_e T_e)]_a$ is the total paleoclassical electron heat flow through the separatrix where $M \rightarrow 0$ and $\Delta P_e(\rho)$ is an integral correction due to net electron heating (or losses via radiation) and convective heat flow between ρ and the separatrix:

$$\Delta P_e(\rho) \equiv \int_\rho^a \frac{d\hat{\rho} V'(\hat{\rho})}{M(\hat{\rho})+1} \left[Q_e^{\text{net}} - \frac{1}{V'} \frac{d}{d\hat{\rho}} \left(V' \frac{5}{2} T_e \Gamma \right) \right]_{\hat{\rho}}. \quad (22)$$

The local heating Q_e^{net} and convective electron heat flux have small effects ($\lesssim 10\%$) in the 98889 pedestal (see Figs. 4a and 5a in Ref. 1) so there $P_e(\rho) \simeq P_e(a) = 1.65 \times 10^6$ W.

The ion energy equation will be considered next. The paleoclassical ion heat transport operator is similar to the electron heat transport operator in (18), except that $M_i \rightarrow 0$ (because there is no helically resonant ion contribution since the ion toroidal precessional drift frequency is usually larger than the ion collision frequency — see discussion after Eq. (139) in Ref. 4). Thus, unlike for paleoclassical electron heat transport, it can be written in the usual heat flux divergence form¹⁷ with $\Upsilon_i^{\text{pc}} = -(1/V')(d/d\rho)[V' \bar{D}_\eta (3/2)n_i T_i]$. Neoclassical ion heat transport can be significant in pedestals.¹ Its ion heat flux will be written as $\Upsilon_i^{\text{nc}} = -n_i \chi_i^{\text{nc}} dT_i/d\rho$. Labeling the anomalous ion heat flux as Υ_i^{an} and performing the same type of analysis as was done for electrons to obtain (20) yields for the ion heat flow equation

$$-\left[\frac{d}{d\rho} \left(V' \bar{D}_\eta \frac{3}{2} n_i T_i \right) \right]_\rho = P_i(\rho) - V' \left[-n_i \chi_i^{\text{nc}} \frac{dT_i}{d\rho} + \Upsilon_i^{\text{an}} \right]_\rho. \quad (23)$$

Here, $P_i(\rho) \equiv P_i(a) - \Delta P_i(\rho)$ is the conductive ion heat flow (W) through the ρ flux surface in which $P_i(a) \equiv -[(d/d\rho)(V' \bar{D}_\eta (3/2)n_i T_e)]_a + V'[-n_i \chi_i^{\text{nc}}(dT_i/d\rho) + \Upsilon_i^{\text{an}}]_a$ is the total ion heat flow through the separatrix. The $\Delta P_i(\rho)$ is analogous to $\Delta P_e(\rho)$ defined in (22) but with helical factor $M_i \rightarrow 0$.

V. ELECTRON DENSITY PROFILE

Deuteron and impurity (e.g., carbon) densities in the pedestal are influenced by differing source, ionization and neoclassical pinch-type effects. These ion complications will be circumvented by solving the simpler electron density equation. Integrating the electron version of (16) radially from ρ to a reference flux surface ρ_{ref} yields

$$[V'\bar{D}_\eta n_e]_\rho = [V'\bar{D}_\eta n_e]_{\rho_{\text{ref}}} + \int_\rho^{\rho_{\text{ref}}} d\hat{\rho} [\dot{N}_e - V'\Gamma^{\text{add}}]_{\hat{\rho}}. \quad (24)$$

Thus, the intrinsic paleoclassical radial density flow $[V'\bar{D}_\eta n_e]$ at ρ is equal to its value on the reference flux surface plus the radial integral from ρ to the reference flux surface of the fueling source \dot{N}_e minus any additional particle loss rate $V'\Gamma^{\text{add}}$ (s^{-1}).

The effect of the fueling source in (24) is often small. For example, at the density mid-point ($\rho_{\text{mid}} \simeq 0.98a$) of the 98889 pedestal the density flow rate $[V'\bar{D}_\eta n_e]_{\rho_{\text{mid}}}/(a - \rho_{\text{mid}}) \simeq (0.98 \times 43.5)(1.6 \times 0.345)(1.77 \times 10^{19})/(0.02a) \simeq 2.7 \times 10^{22} \text{ s}^{-1}$ is large compared to the maximum electron source rate¹ $\dot{N}_e(a) \simeq 2 \times 10^{21} \text{ s}^{-1}$ in this pedestal determined from a combination of 1D and 2D neutral recycling modeling and taking into account the source due to the ionization of carbon impurities:

$$\frac{\int_{\rho_{\text{mid}}}^a d\hat{\rho} \dot{N}_e(\hat{\rho})}{[V'\bar{D}_\eta n_e]_{\rho_{\text{mid}}}} \lesssim \frac{(a - \rho_{\text{mid}}) \dot{N}_e(a)}{[V'\bar{D}_\eta n_e]_{\rho_{\text{mid}}}} \simeq 0.07 \ll 1. \quad (25)$$

Neglecting \dot{N}_e , additional particle loss rates $V'\Gamma^{\text{add}}$ and the slight radial variation of V' , to lowest order (24) becomes $n_e(\rho) \bar{D}_\eta(\rho) \simeq \text{constant}$, or more explicitly

$$n_e(\rho) \simeq n_e(\rho_{\text{ref}}) \frac{\bar{D}_\eta(\rho_{\text{ref}})}{\bar{D}_\eta(\rho)}. \quad (26)$$

This model prediction represents the density profile required to produce a small net paleoclassical density flux Γ^{pc} — by nearly balancing the outward diffusive density flux with a large inward pinch flux in (12). That is, since the fueling source density flow $\int d\hat{\rho} \dot{N}_e$ is typically small relative to the intrinsic paleoclassical density flow $[V'\bar{D}_\eta n_e]$, (26) indicates the density profile the pedestal adjusts itself to in order to produce a small net radial density flux $\Gamma^{\text{net}} = \dot{N}_e/V' \ll [V'\bar{D}_\eta n_e]/(a - \rho_{\text{top}})$ through the pedestal. This scenario is precisely the conclusion of a pioneering interpretive analysis of the ion density pinch and diffusivity²⁹ in the 98889 and another DIII-D pedestal; paleoclassical predictions were found to be consistent with pinch and inferred diffusivity values obtained in the 98889 pedestal (see Figs. 25, 26 in Ref. 1).

If the reference radius ρ_{ref} is taken to be the separatrix at a , then (26) predicts the pedestal density profile is determined by the electron density at the separatrix and just increases from there $\propto 1/\bar{D}_\eta$ as one moves from the

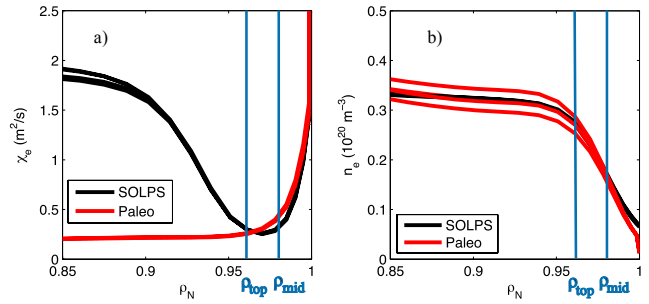


FIG. 2. Comparison of paleoclassical-based pedestal structure model predictions (in red) to interpretive modeling⁵ (in black) for 4 carbon transport models that result in slightly different Z_{eff} profiles for the DIII-D 98889 pedestal:^{1,6} a) effective electron heat diffusivity χ_e and b) density n_e profiles.

separatrix into and up the pedestal. If in addition a^2/\bar{a}^2 is assumed to be constant at a value of 1.6 (i.e., neglecting the weak divergence of this quantity at the separatrix), then the predictions from (26) are $n_e(\rho_{\text{mid}})/n_e(a) \simeq 3.5$ and $n_e(\rho_{\text{top}})/n_e(a) \simeq 6.9$. These ratios are somewhat larger than (but less than a factor of two more than) the corresponding experimental values of 2.3 and 3.6. However, leveraging the pedestal density profile off the density at the separatrix is problematic for a number of reasons: the separatrix location is not accurately known; plasma parameters may not be constant on $\rho_N > 0.99$ flux surfaces;¹ the geometric factors a^2/\bar{a}^2 and $\langle |\nabla\rho|^2 \rangle$ diverge weakly as $\ln q$ there; ion loss-cone orbit losses and ion kinetic effects can become important there; etc.

Qualitative comparisons of the shape of the pedestal electron density profile predicted by (26) have been made to experimental data for the DIII-D 98889 pedestal⁶ (Fig. 2) and in NSTX⁵ (Fig. 3). In these interpretive modeling studies the predicted density profile is scaled so that the average edge density from the model matches the magnitude of the experimental pedestal data. These results show (26) qualitatively captures the experimental trends of the edge density profiles in the DIII-D 98889 discharge⁶ (Fig. 2b), and without and with lithium-coated walls in NSTX⁵ (Fig. 3b). Note that if D_η were spatially constant (e.g., as in a Fick's diffusion law with a constant D), (26) would predict $n_e(\rho) = \text{constant}$ in the pedestal, i.e., no density pedestal at all.

A more fundamental and quantitative test of the pedestal density profile prediction compares its density gradient prediction to experimental data. A density gradient prediction can be obtained by dividing (16) by $[V'\bar{D}_\eta n_e]_\rho$ and splitting up the ρ derivatives to obtain

$$\frac{1}{L_{n_e}} = \frac{1}{L_\eta} + \frac{\dot{N}_e(\rho) - [V'\Gamma^{\text{add}}]_\rho}{[V'\bar{D}_\eta n_e]_\rho}. \quad (27)$$

Here, the electron density gradient scale length L_{n_e} and

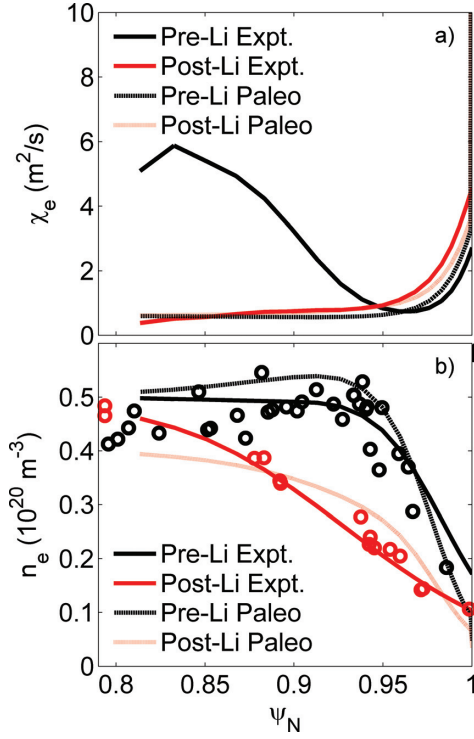


FIG. 3. Comparison of paleoclassical-based pedestal structure model predictions (in red) to SOLPS interpretive modeling⁵ (in black) for NSTX edge regions without (Pre-Li) and with (Post-Li) lithium-coated plasma-facing components: a) effective electron heat diffusivity χ_e and b) density n_e profiles. The radial coordinate Ψ_N here is the normalized poloidal flux.

magnetic field diffusivity scale length L_η are defined by

$$\frac{1}{L_{n_e}} \equiv -\frac{d \ln n_e}{d\rho}, \quad \frac{1}{L_\eta} \equiv \frac{d \ln (V' \bar{D}_\eta)}{d\rho}. \quad (28)$$

The normalized length L_{n_e}/a is approximately equal to half the “width” parameter in ρ space of the relevant tanh fit.¹ For the 98889 pedestal density profile, this yields $L_{n_e}/a \simeq 0.0235$ at $\rho_N = 0.982$.

At the mid-point ($\rho_N \simeq 0.98 a$) of the 98889 pedestal, which is near where the maximum pedestal density gradient occurs, $a/L_{n_e}^{\text{exp}} \simeq 35$ (Fig. 9b in Ref. 1) whereas $a/L_\eta \simeq 50$. Using $\dot{N}_e(\rho_{\text{mid}}) \simeq 6 \times 10^{20} \text{ s}^{-1}$ from Ref. 1, the fueling contribution is found to be small: $[a\dot{N}_e/(V'\bar{D}_\eta n_e)]_{\rho_{\text{mid}}} \simeq 1$. Thus, the density gradient prediction of $1/L_\eta$ is almost 50% larger than $1/L_{n_e}^{\text{exp}}$ here. An additional particle flux $\Gamma^{\text{add}} \simeq 2 \times 10^{20} \text{ m}^{-2} \text{ s}^{-1}$ would be sufficient to obtain agreement. Assuming a Fick’s diffusion law model, the FSA density flux can be written as¹ $\Gamma^{\text{add}} = \langle |\nabla \rho|^2 \rangle D^{\text{add}} n_e / L_{n_e}$. For such a model $D^{\text{add}}(\rho_{\text{mid}}) \simeq 0.12 \text{ m}^2 \text{ s}^{-1}$ is required to obtain agreement between the prediction for $1/L_\eta$ in (27) and the experimental value. It is small compared to the $D_\eta \simeq 0.345 \text{ m}^2 \text{ s}^{-1}$ at ρ_{mid} . Thus, while some additional density flux (from collisional or microturbulence processes) may be needed for precise agreement, this paleoclassical-based

density transport model can apparently capture the dominant features of the pedestal density profile — its approximate (factor < 2) magnitude, shape and maximum gradient.

As indicated in (9), the magnetic field diffusivity D_η in pedestals varies as $Z_{\text{eff}}/T_e^{3/2}$ times a function of the electron collisionality parameter $\nu_{*e}(T_e, Z_{\text{eff}}, n_e)$. Thus, it depends strongly on the yet to be determined T_e profile. A general scaling relation for n_e cannot be developed from (26). However, since D_η is mainly a function of T_e , the n_e and T_e profiles should be “aligned” (i.e., strongly correlated) whenever local fueling and possible additional density flux effects are small. This observation qualitatively agrees with most experimental H-mode pedestal data (cf., Fig. 1). When the fueling and additional transport effects are significant, (27) indicates that while fueling due to \dot{N}_e should increase the predicted density gradient, any additional density transport flux Γ^{add} should decrease it.

While fueling effects are negligible in the 98889 pedestal, they can become significant when neutral beam (NB) core heating and fueling, and consequently edge recycling, are large. Neutral fueling effects apparently decrease the pedestal density width slightly at high density in DIII-D^{30,31} but have less effect in Alcator C-Mod (C-Mod).³² The relative importance of Γ^{add} may also change with plasma parameters. Outward shifts of the n_e profile relative to the T_e profile in the pedestal have been observed in the high NB power (and high toroidal field, low ϱ_* , high density) DIII-D data in dimensionless variable comparison experiments with the Joint European Torus (JET) experiment.³³ In contrast, in JET the pedestal profiles of n_e and T_e are usually more aligned — perhaps because possible density fluxes due to \dot{N}_e/V' and Γ^{add} are smaller relative to the intrinsic level $\bar{D}_\eta n_e / L_{n_e}$ of the paleoclassical FSA density transport flux in JET.

Finally, processes that limit the height of the density pedestal will be considered assuming fueling and additional density flux effects are small. In moving radially inward from the separatrix, D_η decreases as T_e increases, but becomes nearly constant as T_e “saturates” (e.g., for $\rho_N \lesssim \rho_{\text{top}}/a = 0.96$ in Fig. 1). When this effect dominates [e.g., when $d \ln \bar{D}_\eta / d\rho \lesssim 10/a$], n_e at the pedestal top would be predicted by (26). Such a situation may be occurring for $\rho \lesssim \rho_{\text{top}}$ in the DIII-D 98889 modeling results shown in Fig. 2b and in the analyzed NSTX discharges shown in Fig. 3b (for the NSTX T_e and other profiles see Fig. 2 in Ref. 5).

Although apparently not needed in the comparisons in Figs. 2b and 3b, microturbulence-induced anomalous density transport presumably becomes dominant as one moves from the pedestal into the core. Assuming a Fick’s diffusion law $\Gamma^{\text{add}} = -\langle |\nabla \rho|^2 \rangle D^{\text{an}} dn_e / d\rho$ in (16), one needs only $D^{\text{an}} \gtrsim [(a^2/\bar{a}^2)/\langle |\nabla \rho|^2 \rangle] D_\eta$ ($\sim 0.14 \text{ m}^2 \text{ s}^{-1}$ at the top of the 98889 pedestal) for anomalous density transport to become dominant and thereby determine the density at ρ_{top} . A scaling relation for testing this possible limit on the pedestal density height could be

developed from $D^{\text{an}} \sim D_\eta$ if and when a formula for the microturbulence-induced D^{an} near the pedestal top becomes available.

VI. ELECTRON TEMPERATURE PROFILE

The pedestal density profile analysis in the preceding section was incomplete in that the D_η profile, which depends strongly on the electron temperature profile $T_e(\rho)$, was not determined there. This section uses various approximations in and integrals of (20) to predict a number of properties of the T_e profile in an H-mode pedestal.

Neglecting any possible additional electron heat flux Υ_e^{add} in the pedestal and using (16), the electron heat flow equation in (20) can be written as

$$-[V'\bar{D}_\eta n_e] \frac{3}{2} \frac{dT_e}{d\rho} = P_e(\rho) - \frac{3}{2} T_e (\dot{N}_e - V'\Gamma^{\text{add}}). \quad (29)$$

Electron heat lost via the fueling term is often negligible compared to conductive electron heat flow through the pedestal: $(3/2)\dot{N}_e T_e / P_e \sim (1.5)(2 \times 10^{21})(89)(1.6 \times 10^{-19}) / (1.65 \times 10^6) \simeq 0.025$ at the separatrix in the 98889 pedestal. Thus, neglecting the \dot{N}_e and Γ^{add} terms on the right of (29), the electron temperature profile is determined to lowest order by

$$-\frac{dT_e}{d\rho} = \frac{P_e}{(3/2)[V'\bar{D}_\eta n_e]} \simeq \text{spatially constant}. \quad (30)$$

Physically, this model prediction represents the electron temperature gradient required to carry the electron conductive power P_e through the pedestal region when paleoclassical radial electron heat transport is dominant.

Because local electron heating Q_e^{net} and electron convective heat flow are often negligible compared to electron heat flow through the pedestal, $\Delta P_e \ll P_e$ and hence $P_e(\rho) \simeq P_e(a)$ is often nearly constant there. Also, from (26) the combination of parameters $[V'\bar{D}_\eta n_e]$ is predicted to be approximately constant in pedestals. Hence, (30) predicts the electron temperature gradient is nearly constant in H-mode pedestals — until significant Υ_e^{add} anomalous electron heat transport is encountered in moving from the pedestal into the core plasma,¹ which will be discussed at the end of this section.

Electron temperature gradients frequently appear to be roughly spatially constant within many H-mode pedestals (cf., Fig. 1b). But uncertainties in the data usually prevent a firm conclusion about the degree of constancy of $dT_e/d\rho$. The near constancy of P_e and $[V'\bar{D}_\eta n_e]$ also means that experimental validation tests of the prediction for $dT_e/d\rho$ in (30) can be made at any flux surface in the steep T_e gradient region (II, III) of the pedestal.

The electron temperature gradient prediction in (30) could in principle be integrated using a D_η formula such as that specified in (9). However, since $dT_e/d\rho$ is predicted to be nearly constant in space, the predicted T_e

profile is simply $T_e(\rho) \simeq T_e(a) + (a - \rho)[-dT_e/d\rho]$, which should apply from the separatrix in to near the top of the pedestal. Using this T_e profile in formulas for D_η given in (1)–(8) or (9), the n_e profile and its gradient could then, in principle, be predicted from (26) or (24).

In order to quantitatively compare the electron temperature gradient prediction in (30) to experimental data, it is useful to convert it to a prediction for the electron temperature gradient scale length. Dividing (30) by T_e and multiplying it by a yields a prediction for the normalized electron temperature gradient scale length:

$$\frac{L_{T_e}}{a} \equiv \left[-\frac{a}{T_e} \frac{dT_e}{d\rho} \right]^{-1} = \frac{(3/2)[V'\bar{D}_\eta n_e]_\rho T_e(\rho)}{a P_e(\rho)}. \quad (31)$$

At the mid-point $\rho_{\text{mid}} = 0.98a$ of the 98889 pedestal this yields a prediction of $L_{T_e}/a \simeq 0.028$, which is only 40% larger than the experimental value of $L_{T_e}^{\text{exp}}/a \simeq 0.02$ (see Fig. 9b in Ref. 1). The tanh fit width parameter for the 98889 pedestal yields $L_{T_e}/a \simeq 0.0215$ at $\rho_N \simeq 0.978$.

Using the $dT_e/d\rho$ prediction in (30), the effective electron heat diffusivity defined by Eq. (13) in Ref. 1 is

$$\chi_{e\text{eff}}^{\text{pc}} \equiv \frac{P_e}{V'(|\nabla\rho|^2)(-n_e dT_e/d\rho)} = \frac{a^2/\bar{a}^2}{\langle|\nabla\rho|^2\rangle} \frac{3}{2} D_\eta. \quad (32)$$

In the regions II and III of the 98889 pedestal, $a^2/\bar{a}^2 \simeq 1.6$ and $\langle|\nabla\rho|^2\rangle \simeq 2$; thus, the prediction is that $\chi_{e\text{eff}}^{\text{pc}} \simeq 1.2 D_\eta$ there. This $\chi_{e\text{eff}}^{\text{pc}}$ prediction in the pedestal region is different from the usual local paleoclassical estimate⁴ of $\chi_e^{\text{pc}} \simeq (3/2)(M+1)D_\eta$ because of the non-standard structure of the paleoclassical electron heat transport operator shown in (18) and because there is very little net local electron heating or cooling in the pedestal — electron heat just flows radially through the pedestal.

Comparisons of the $\chi_{e\text{eff}}^{\text{pc}}$ profiles to the χ_e 's obtained from SOLPS interpretive transport analysis^{1,5} in the edge region are shown for the DIII-D 98889 discharge in Fig. 2a and for the NSTX discharges in Fig. 3a. The SOLPS modeling (see Section 2 of Ref. 5 and Ref. 1 for details) determines the effective electron heat diffusivity χ_e that is required to reproduce the measured profiles, while self-consistently including the contributions of neutrals and radiation. As shown in Fig. 3a, the paleoclassical-based prediction in (32) captures much of the structure seen in the steep gradient region of NSTX pedestals, with χ_e being similar in magnitude and increasing strongly with radius there. Furthermore, $\chi_{e\text{eff}}^{\text{pc}}$ exhibits the modest increases there in the lithium-coated wall discharges compared to the NSTX discharges without lithium. In the pedestal-top region, Fig. 3a shows the experimental χ_e is significantly higher than $\chi_{e\text{eff}}^{\text{pc}}$ for the NSTX discharges without lithium, suggesting that another transport mechanism dominates there; in discharges with lithium, the agreement with $\chi_{e\text{eff}}^{\text{pc}}$ agrees well over the entire edge region ($\Psi_N \gtrsim 0.82$). Fig. 2a shows that for the DIII-D 98889 pedestal the $\chi_{e\text{eff}}^{\text{pc}}$ profile for $\rho \gtrsim \rho_{\text{top}} = 0.96a$ closely mirrors the experimentally-inferred χ_e profile,

but additional electron heat transport is needed in the pedestal-top region.

The possible effect of ETG-induced anomalous electron heat transport^{34,35} will be considered next. Near the pedestal top the combination of parameters $[V'\bar{D}_\eta n_e]$ is nearly constant (on the L_{T_e} scale length) — not because of (26) but because each of its parameters is individually nearly constant there. Assuming M does not vary rapidly there and $\Upsilon_e^{\text{add}}(a) \simeq 0$, the electron energy flow equation in (20) can be simplified near ρ_{top} to approximately

$$-V'\bar{D}_\eta n_e \frac{3}{2} \frac{dT_e}{d\rho} + \frac{1}{M+1} V'\Upsilon_e^{\text{an}} \simeq P_e(\rho). \quad (33)$$

A formula for the anomalous electron heat flux induced by ETG-driven microturbulence is needed to proceed further. To the author's knowledge no such expression is available for the near separatrix geometry and pedestal plasma parameters. However, one can be constructed from results of the gyrokinetic-based numerical simulations of ETG-induced microturbulence by Jenko et al.³⁶ at the top of an Asdex Upgrade (AUG) H-mode pedestal³⁷ that has parameters similar to the DIII-D 98889 pedestal.¹ From Table I in Ref. 36, at this AUG pedestal's top $\eta_e \equiv d \ln T_e / d \ln n_e = L_{n_e} / L_{T_e} = \omega_{T_e} / \omega_n = 24.8 / 11.2 \simeq 2.2$; similarly, Fig. 10b in Ref. 1 indicates that $\eta_e \gtrsim 2$ for $\rho \lesssim \rho_{\text{top}}$ in the 98889 pedestal. Thus, from Fig. 7 in Ref. 36 since $\eta_e \gg \eta_{e,\text{crit}} \simeq 1.2$ (see Ref. 35), one is apparently well beyond the ETG threshold regime and in a nearly asymptotic ETG regime where χ_e^{ETG} no longer increases much with η_e . Hence, threshold-type ETG transport effects are apparently not important at the top of the pedestal and one can approximate the ETG-induced anomalous electron heat transport by a standard Fourier heat flux law in the form $\Upsilon_e^{\text{ETG}} = -n_e \langle |\nabla \rho|^2 \rangle \chi_e^{\text{ETG}} dT_e / d\rho$.

For AUG parameters the ETG simulations³⁶ found $\chi_e^{\text{ETG}} \simeq 0.83 \text{ m}^2 \text{ s}^{-1}$, which is a factor of about two larger than the $\chi_e \sim 0.4 \text{ m}^2 \text{ s}^{-1}$ obtained from interpretive transport analysis.^{36,37} Using parameters for this AUG pedestal of $T_e \simeq 0.69 \text{ keV}$, $L_{T_e} = a / \omega_{T_e} \simeq 0.65 / 24.8 \simeq 0.026 \text{ m}$ and toroidal field strength $B_t \simeq 2.4 \text{ T}$, in terms of an anticipated electron gyroBohm diffusivity $\chi_e^{\text{gB}} \equiv (\sqrt{T_e / m_e} / \omega_{ce} L_{T_e}) (T_e / e B_t)$ this ETG-induced electron heat diffusivity is $\chi_e^{\text{ETG}} \simeq 3 \chi_e^{\text{gB}}$; the numerical factor would be $\simeq 1.4$ if the interpretive analysis χ_e were used. Thus, one infers

$$\begin{aligned} \chi_e^{\text{ETG}} &\simeq c_\# \chi_e^{\text{gB}} \equiv c_\# \frac{\sqrt{T_e / m_e} / \omega_{ce}}{L_{T_e}} \frac{T_e}{e B_t} \\ &\simeq 0.075 c_\# \frac{[T_e(\text{keV})]^{3/2}}{L_{T_e}(\text{m}) B_t(\text{T})^2} \frac{\text{m}^2}{\text{s}}, \end{aligned} \quad (34)$$

in which from the AUG pedestal transport analysis³⁷ or simulations³⁶ the coefficient $c_\# \simeq 1.4$ or 3.

The effect of the resultant anomalous electron heat flux Υ_e^{ETG} in (33) will now be considered. While $\chi_e^{\text{ETG}} \propto T_e^{3/2}$, $\chi_e^{\text{pc}} \simeq (3/2) M D_\eta \propto T_e^{1/2}$ increases more slowly with increasing T_e since at the

pedestal top $M \simeq \lambda_e / \pi R_0 q \propto T_e^2$ ($M \simeq 3.1$ at $\rho_{\text{top}} \simeq 0.96 a$ in the 98889 pedestal). Thus, ETG-induced anomalous electron heat transport will begin to “saturate” the increase in T_e and reduce the electron temperature gradient when $\langle |\nabla \rho|^2 \rangle \chi_e^{\text{ETG}} \gtrsim (a^2 / \bar{a}^2) \chi_e^{\text{pc}} \simeq (a^2 / \bar{a}^2) (3/2) (\sqrt{2 T_e} / m_e / \pi R_0 q) \delta_e^2$ in which⁴ $\delta_e \equiv c / \omega_{pe} \propto 1 / \sqrt{n_e}$ is the electromagnetic skin depth. Equating these electron heat diffusivities yields an approximate prediction for the electron pressure $p_e \equiv n_e T_e$ at the pedestal top:

$$\beta_e^{\text{ped}} \equiv \frac{n_e^{\text{ped}} T_e^{\text{ped}}}{B_t^2 / 2 \mu_0} \sim \frac{3\sqrt{2}}{\pi c_\#} \frac{a^2 / \bar{a}^2}{\langle |\nabla \rho|^2 \rangle} \frac{\eta_{\parallel}^{\text{nc}}}{\eta_0} \left(\frac{L_{T_e}}{R_0 q} \right). \quad (35)$$

This is just a rough criterion for where T_e begins to saturate with decreasing ρ near the T_e pedestal top. A more approximate pedestal height prediction than (35) that used a more generic gyroBohm scaling for χ_e^{an} was given previously in the last paragraph of Section 6 in Ref. 13.

At the top ($\rho_{\text{top}} \simeq 0.96 a$) of the 98889 pedestal $L_{T_e}^{\text{exp}} \simeq 0.06 a \simeq 0.046 \text{ m}$ (see Fig. 9b in Ref. 1) and $q \simeq 4.4$, so (35) predicts $\beta_e^{\text{ped}} \simeq 0.0056 / c_\#$. For $c_\# \sim 1.4\text{--}3$ this is within about a factor of two of the experimental value of $\beta_e^{\text{exp}}(\rho_{\text{top}}) \simeq 0.0018$. The ETG electron heat diffusivity estimated from (34) at $\rho_{\text{top}} \simeq 0.96 a$ in the 98889 pedestal is $\chi_e^{\text{ETG}} \sim 0.31\text{--}0.66 \text{ m}^2 \text{ s}^{-1}$, which is of order the strongly spatially varying interpretive transport results there (see Fig. 8a of Ref. 1).

Since the T_e gradient scale length L_{T_e} is often roughly constant at about 2.5–4% of the minor radius a (see for example Figs. 4a and 11a in Ref. 28), (35) predicts that at constant B_t and q , the pedestal electron temperature T_e^{ped} should scale inversely with the pedestal density n_e^{ped} : $T_e^{\text{ped}} \sim 1 / n_e^{\text{ped}}$. Such a scaling has been observed in AUG (Fig. 12 in Ref. 38), JET (Figs. 26–28 in Ref. 39), DIII-D (Fig. 4 in Ref. 40), C-Mod (Fig. 10 in Ref. 41) and Japan Torus JT-60U (Fig. 7a in Ref. 42). However, quantitative comparisons to (35) remain to be made.

VII. ION TEMPERATURE PROFILE

Ion heat transport in pedestals is apparently¹ a complicated mix of neoclassical plus paleoclassical contributions throughout, possible kinetic effects in the pedestal's region III and transitions to ion-temperature-gradient (ITG)-driven anomalous transport in the core (I). Also, kinetic effects due to ion banana drift orbits could modify $dT_i / d\rho$ very near the separatrix and even render T_i an inappropriate measure of ion energy in region III.

Nonetheless, neglecting Υ_i^{an} , $(3/2) N_i T_i$ fueling effects and kinetic effects in (23), the pedestal ion temperature gradient is predicted to be

$$-\frac{dT_i}{d\rho} \simeq \frac{P_i(\rho)}{V' n_i [(3/2) \bar{D}_\eta + \chi_i^{\text{nc}}]}. \quad (36)$$

Since the sum of the terms in the denominator does not vary much in the pedestal (\lesssim factor of 2 in the

98889 pedestal — see Fig. 11 in Ref. 1), the predicted ion temperature gradient may also be approximately constant in the pedestal. Similar to (32), the effective paleoclassical ion heat diffusivity can be determined from (36) by omitting χ_i^{nc} in it which yields $\chi_{i\text{eff}}^{\text{pc}} = (3/2) [(a^2/\bar{a}^2)/\langle|\nabla\rho|^2\rangle] D_\eta$.

Dividing (36) by T_i/a and inverting it yields a prediction for the ion temperature gradient scale length:

$$\frac{L_{T_i}}{a} \equiv \left[-\frac{a}{T_i} \frac{dT_i}{d\rho} \right]^{-1} \simeq \frac{[(3/2)\bar{D}_\eta + \chi_i^{\text{nc}}]n_i T_i}{a P_i/V'}. \quad (37)$$

At the mid-point of the 98889 pedestal¹ where $n_i/n_e \simeq 0.635$, $T_i \simeq 512$ eV, $\chi_i^{\text{nc}} \simeq 0.43$ m² s⁻¹ and the conductive $P_i \simeq 0.56 \times 10^6$ W, (37) yields $[L_{T_i}/a]_{\rho_{\text{mid}}} \simeq 0.11$, which is about a factor of two larger than the experimental $[L_{T_i}/a]_{\rho_{\text{mid}}}^{\text{exp}} \simeq 0.05$ (see Fig. 9b in Ref. 1). Since it was noted in Ref. 1 that the estimate of the neoclassical ion heat diffusivity used there may be 30% too large in the pedestal region, the $[L_{T_i}/a]_{\rho_{\text{mid}}}$ prediction may actually be somewhat closer to the experimental value.

Determination of the “top” of the T_i pedestal is even more problematic than for T_e — see discussion around Eq. (35) above. This is because firstly the pedestal ion temperature profile often does not have a very well defined point where its gradient changes significantly (cf., the T_i profile in Fig. 1), which would be indicative of a transition in the dominant ion heat transport process. Secondly, unlike with ETG-driven anomalous transport, ITG-driven anomalous transport is likely to be at or near threshold conditions in which case a simple Fourier heat flux law is not appropriate.

VIII. TOROIDAL FLOW PROFILE AND RADIAL ELECTRIC FIELD

Plasma flows are just beginning to be understood in H-mode pedestals. The poloidal ion flow V_p should be determined^{16,17} by ion neoclassical poloidal flow damping on the ion-ion collision time scale (\sim ms)²⁰ since anomalous ion poloidal flow processes are apparently not significant in pedestals.¹ For deuterons it is predicted to be $V_{pi} \simeq (c_p/q_i B_t)(dT_i/d\rho)$, in which $c_p \equiv k_i \sim 1$ ($k_i \simeq 1.17$ for $\nu_{*i} \ll 1$, $\sqrt{\epsilon} \ll 1$ and $Z_{\text{eff}} = 1$) is a factor determined by neoclassical theory,²⁰ which can be evaluated using NCLASS.²³ Early measurements⁴³ indicated dominant ion (helium) poloidal flows larger than neoclassical theory predicted; however, charge-exchange frictional drag may have been important there.⁴⁴ Recent measurements of poloidal impurity ion flows in C-Mod,^{45,46} MAST,⁴⁷ NSTX⁴⁸ and DIII-D⁴⁹ pedestals are of order neoclassical predictions but often have large error bars that prevent definitive conclusions.

Recently a comprehensive transport time scale (\sim fractions of a second) equation has been developed^{16,17,50} for the total plasma toroidal rotation frequency $\Omega_t \equiv L_t/(m_i n_i (R^2)) \simeq V_t/R$ where $L_t \equiv m_i n_i \langle \mathbf{e}_\zeta \cdot \mathbf{V} \rangle =$

$\sum_{\text{ions}} m_s n_s \langle \mathbf{e}_\zeta \cdot \mathbf{V}_s \rangle$ is the total plasma toroidal angular momentum density in which $\mathbf{e}_\zeta \equiv R \hat{\mathbf{e}}_\zeta$ is the toroidal angular momentum vector. That is, toroidal flows of the dominant hydrogenic ion and impurity species are added together and Ω_t will represent the total plasma toroidal angular rotation frequency. Separate toroidal flows of the dominant hydrogen ions and the impurities can be obtained from NCLASS calculations using the determined Ω_t (radial electric field^{16,50} — see Eq. (45) below).

In a transport quasi-equilibrium the flux surface average (FSA) toroidal plasma rotation equation can be simplified to^{16,17,50,51}

$$0 = -\langle \mathbf{e}_\zeta \cdot \nabla \cdot \boldsymbol{\pi}_{i\parallel}^{3D} \rangle + \sum_{m,n} \langle \mathbf{e}_\zeta \cdot \overline{\delta \mathbf{J}_{\parallel m/n} \times \delta \mathbf{B}_{\rho m/n}} \rangle - \langle \mathbf{e}_\zeta \cdot \nabla \cdot \boldsymbol{\pi}_{i\perp} \rangle - \frac{1}{V'} \frac{d}{d\rho} (V' \Pi_{i\rho\zeta}) + \langle \mathbf{e}_\zeta \cdot \bar{\mathbf{S}}_m \rangle. \quad (38)$$

Here, $\boldsymbol{\pi}_{i\parallel}^{3D}$ is the parallel ion viscous stress induced by non-resonant three-dimensional (3D) magnetic field effects, the second term represents the localized torques induced in the vicinity of rational surfaces ($q = m/n$) caused by the resonant components of 3D $\delta \mathbf{B}$ fields, $\boldsymbol{\pi}_{i\perp}$ is the perpendicular ion stress due to collision-induced classical, neoclassical and paleoclassical processes, $\Pi_{i\rho\zeta}$ is the ρ, ζ component of the microturbulence-induced Reynolds ion stress tensor and $\langle \mathbf{e}_\zeta \cdot \bar{\mathbf{S}}_m \rangle$ is the FSA toroidal torque density applied to the plasma at this flux surface by net momentum sources and sinks (losses) $\bar{\mathbf{S}}_m$.

Neglecting effects due to non-resonant and resonant 3D magnetic fields and fluctuation-induced Reynolds stress which are often small in H-mode pedestals, this equation becomes simply $\langle \mathbf{e}_\zeta \cdot \nabla \cdot \boldsymbol{\pi}_{i\perp} \rangle \simeq \langle \mathbf{e}_\zeta \cdot \bar{\mathbf{S}}_m \rangle$. The collision-induced perpendicular ion stress is dominated by its paleoclassical component,¹⁶ which yields an effective toroidal momentum diffusivity $\chi_{t\text{eff}}^{\text{pc}} \equiv \bar{D}_\eta / \langle |\nabla\rho|^2 \rangle$. Thus, using the paleoclassical toroidal torque given by Eq. (103) in Ref. 16, the lowest order equation becomes

$$-\frac{1}{V'} \frac{d^2}{d\rho^2} [V' \bar{D}_\eta L_t] \simeq \langle \mathbf{e}_\zeta \cdot \bar{\mathbf{S}}_m \rangle. \quad (39)$$

Multiplying by V' and integrating over ρ yields an equation analogous to the density flow equation in (16) or the electron energy flow equation in (20):

$$-\left[\frac{d}{d\rho} (V' \bar{D}_\eta L_t) \right]_\rho \simeq V'(\rho) \Pi_t(\rho). \quad (40)$$

Here, $V'(\rho) \Pi_t(\rho) = V'(a) \Pi_t(a) - V'(a) \Delta \Pi_t(\rho)$ is the toroidal angular momentum flow rate (torque, N m), which is comprised of the flow of L_t through the separatrix $V'(a) \Pi_t(a) \equiv -[(d/d\rho)(V' \bar{D}_\eta L_t)]_a$ plus an integral correction $V'(a) \Delta \Pi_t(\rho) \equiv \int_\rho^a d\hat{\rho} V'(\hat{\rho}) \langle \mathbf{e}_\zeta \cdot \bar{\mathbf{S}}_m \rangle_{\hat{\rho}}$ due to plasma toroidal momentum sources and losses between the ρ flux surface and the separatrix.

In low density pedestals with modest, primarily core NB torque applied to the plasma and small charge exchange losses (e.g., from fueling dominantly from the

X-point region rather than from the main chamber wall, such as in the 98889 pedestal¹), the $V'\Pi_t$ term on the right side of (40) can be neglected. Then, (40) becomes simply $[(d/d\rho)(V'\bar{D}_\eta L_t)]_\rho \simeq 0$. Analogous to the density profile analysis discussion between (24) and (26), this equation indicates that $V'\bar{D}_\eta L_t \simeq V'\bar{D}_\eta \sum_{\text{ions}} m_s n_s \langle R^2 \rangle \Omega_t \simeq \text{constant}$. Neglecting the small variations of V' and $\langle R^2 \rangle$ in the pedestal and using the relation in (26) assuming $\sum_{\text{ions}} n_s m_s / n_e \simeq \text{constant}$, this last relation yields

$$\boxed{\Omega_t(\rho) \simeq \text{constant} \implies \Omega_t(\rho) \simeq \Omega_t(a)}. \quad (41)$$

Thus, to lowest order the total toroidal plasma flow $V_t \simeq R\Omega_t$ is predicted to be approximately spatially constant within the pedestal — at its value on the separatrix. Hence, in this model the separatrix V_t boundary condition (usually > 0) is carried inward from the separatrix to the pedestal top. Toroidal flow of the carbon species was found to be nearly constant in the pedestal region in both the 98889 and a similar 119436 DIII-D pedestal,^{29,52} in qualitative agreement with this prediction.

Possible effects of radial flow of L_t through the pedestal and momentum sources and losses can be quantified by integrating (40) from ρ to the separatrix at a to yield

$$[V'\bar{D}_\eta L_t]_\rho \simeq [V'\bar{D}_\eta L_t]_a + \int_\rho^a d\hat{\rho} V'(\hat{\rho}) \Pi_t(\hat{\rho}). \quad (42)$$

In high density pedestals with large charge-exchange momentum losses (e.g., due to main chamber wall recycling) and modest applied plasma torques (e.g., in EC heated H-mode plasmas or with weak NBs), one can have a situation where radial flow of L_t from the core into the pedestal is small and momentum loss via charge exchange dominates.

The possible effects of charge-exchange-induced momentum losses will be represented by $\langle \mathbf{e}_\zeta \cdot \bar{\mathbf{S}}_m \rangle \simeq -\nu_{\text{cx}} L_t \equiv -\sum_{\text{ions}} m_s n_s \nu_{\text{cxs}} (\mathbf{e}_\zeta \cdot \mathbf{V}_s)$. Then, when Ω_t is positive (co-current directed) on the separatrix, charge-exchange momentum losses in the pedestal require a radial flow of L_t inward (i.e., < 0) across the separatrix. This situation can be modeled by representing the charge exchange momentum loss by $\nu_{\text{cx}}(\rho) L_t(\rho) \simeq \nu_{\text{cx}}(a) L_t(a) e^{-(a-\rho)/\lambda_n}$. Then, assuming the edge region with minimal radial flow of L_t into it from the core is wider than the neutral penetration depth λ_n , the inward momentum flow across the separatrix estimated by setting $V'\Pi_t$ from (40) to zero for $a - \rho \gg \lambda_n$ yields $V'(a) \Pi_t(a) \equiv -[(d/d\rho)(V'\bar{D}_\eta L_t)]_a = -\lambda_n \nu_{\text{cx}}(a) L_t(a) V'(a)$. Using this result and neglecting the small radial variation of V' , close to the separatrix where $\lambda_n \gg a - \rho$, (42) can be simplified to

$$\Omega_t(\rho) \simeq \Omega_t(a) [1 - (a - \rho) \lambda_n \nu_{\text{cx}}(a) / \bar{D}_\eta(a)]. \quad (43)$$

Thus, charge-exchange-induced momentum losses cause Ω_t to decrease linearly with distance in from its value on the separatrix; i.e., they cause $d\Omega_t/d\rho = [\lambda_n \nu_{\text{cx}}(a) / \bar{D}_\eta(a)] \Omega_t(a) > 0$ in the pedestal.

This prediction is qualitatively consistent with recent results in DIII-D EC heated H-mode plasmas⁵³ and experimental exploration of multiple ion species cases with $dV_{ti}/d\rho > 0$ in AUG pedestals.⁵⁴ If this interpretation that $d\Omega_t/d\rho \propto \lambda_n \nu_{\text{cx}}$ is caused by charge exchange momentum loss effects is validated experimentally, perhaps this could be used as a measure of the degree of neutral recycling that is operative in specific H-mode pedestals.

At the top of the n_e, T_e pedestal, radial transport of plasma toroidal angular momentum presumably transitions to being determined by ITG-induced microturbulence which can produce a significant ion Reynolds stress component $\Pi_{i\rho\zeta}$ in the core plasma. In the absence of a specific prediction for $\Pi_{i\rho\zeta}$ it is difficult to develop a prediction for how $d\Omega_t/d\rho$ might change and precisely where. Assuming $\Pi_{i\rho\zeta} \sim -\langle |\nabla\rho|^2 \rangle \chi_t^{\text{an}} dL_t/d\rho$, at the radius where ITG-induced microturbulence causes $\langle |\nabla\rho|^2 \rangle \chi_t^{\text{an}} \gtrsim \bar{D}_\eta$, integration of (38) from $\rho = 0$ to $\rho \sim \rho_{\text{top}}$ indicates the rotation profile gradient should change to some finite value: $d\Omega_t/d\rho < 0$ for co-current core momentum input $\langle \mathbf{e}_\zeta \cdot \bar{\mathbf{S}}_m \rangle > 0$ or $d\Omega_t/d\rho > 0$ for counter-current core momentum input.

On the outboard midplane of a tokamak the pedestal region is close to the discrete magnetic-field-producing coils and possible magnetic field errors. Thus, 3D magnetic field $\delta\mathbf{B}$ components are largest there and can cause additional toroidal torques on the pedestal plasma. The most important mechanisms there are⁵¹ those due to direct losses of ions or electrons, resonant $\delta\mathbf{J} \times \delta\mathbf{B}$ torques and neoclassical toroidal viscous damping of Ω_t .

Ions trapped in the toroidal magnetic field ripple can drift radially out of the plasma edge. This “ion direct loss” current $\langle \mathbf{J}_{\text{idl}} \cdot \nabla\psi_p \rangle$ induces a radial “return current”^{16,51,55} in the plasma. Here, ψ_p is the poloidal magnetic flux for which $\psi'_p \equiv d\psi_p/d\rho \simeq B_p R$. When this radially inward (negative) plasma return current is crossed with the poloidal magnetic field $\mathbf{B}_p \equiv \nabla\zeta \times \nabla\psi_p$, it induces^{16,51} a toroidal torque $\langle \mathbf{e}_\zeta \cdot \bar{\mathbf{S}}_m \rangle = -\langle \mathbf{J}_{\text{idl}} \cdot \nabla\rho \rangle \psi'_p < 0$ on the plasma in the counter-current direction, which reduces the toroidal plasma rotation in the pedestal. Experiments in JET observed a decreasing toroidal flow Mach number in the edge plasma as the magnetic field ripple was increased (see Fig. 6 in Ref. 33), in qualitative agreement with this prediction.

Conversely, when resonant magnetic perturbations (RMPs) were added to low collisionality DIII-D H-mode plasmas the toroidal plasma rotation in the edge region increased (see Fig. 6h in Ref. 56). This response is as would be predicted if RMPs caused magnetic stochasticity in the pedestal region with attendant electron direct losses⁵⁷ so $\langle \mathbf{e}_\zeta \cdot \bar{\mathbf{S}}_m \rangle = -\langle \mathbf{J}_{\text{edl}} \cdot \nabla\psi_p \rangle > 0$ creates a co-current toroidal torque there; alternatively, the resonant RMP components that create singular layer toroidal torques^{16,51} $\langle \mathbf{e}_\zeta \cdot \delta\mathbf{J}_{\parallel m/n} \times \delta\mathbf{B}_{\rho m/n} \rangle$ in the vicinity of the rational surfaces could also increase Ω_t in the edge plasma. And as indicated in Eqs. (113) and (125) in Ref. 16, both of these processes also increase the net ambipolar radial density flux. Thus, these pro-

cesses provide a qualitative interpretation for the concomitant RMP-induced density pumpout observed in these experiments.^{56,70}

Neoclassical toroidal viscosity (NTV) effects due to non-resonant 3D magnetic fields (from error fields, I-coils and toroidal field ripple) cause a FSA toroidal torque on plasma ions of the generic form^{16,50,51}

$$-\langle \mathbf{e}_\zeta \cdot \nabla \cdot \boldsymbol{\pi}_{i\parallel}^{3D} \rangle \simeq -\mu_{\parallel} (1 - \Omega_*/\Omega_t) (\delta B_n^{3D}/B_t)^2 L_t, \\ \Omega_* \simeq \frac{c_p + c_t}{q_i R B_p} \frac{dT_i}{d\rho} < 0. \quad (44)$$

The order unity numerical coefficient $c_p + c_t$ is determined by the specific 3D radial banana center or ripple-induced drift process and ion collisionality regime involved.^{50,51} NTV effects due to non-resonant 3D field components damp plasma toroidal rotation toward a counter-current-directed $\Omega_* \propto dT_i/d\rho < 0$. Thus, both ripple-trapped ion direct losses and NTV effects decrease a positive plasma toroidal rotation frequency Ω_t in the pedestal. They can even cause Ω_t to become negative and approach $\Omega_* < 0$ for very large NTV effects.^{58,59}

Determining the Ω_t profile in the pedestal when paleoclassical, charge-exchange-induced momentum losses, 3D field effects and charged particle direct losses are all present requires detailed numerical solutions of (38) for L_t . Once the toroidal plasma rotation frequency $\Omega_t \equiv L_t/m_i n_i \langle R^2 \rangle$ is known, the radial electric field is determined from radial ion force balance which yields^{16,51}

$$E_\rho \equiv -\hat{\mathbf{e}}_\rho \cdot \nabla \Phi_0 = |\nabla \rho| \left(\Omega_t \psi'_p + \frac{1}{n_i q_i} \frac{dp_i}{d\rho} - \frac{c_p}{q_i} \frac{dT_i}{d\rho} \right), \quad (45)$$

in which $\hat{\mathbf{e}}_\rho \equiv \nabla \rho / |\nabla \rho|$ is the radial unit vector.

Near the separatrix the plasma toroidal rotation is often observed to be small — compared to the other terms in (45). Presumably this is because sheath effects along open field lines in the scrape-off-layer (SOL) outside the separatrix cause a large radial electric field there of $E_\rho \sim T_e(a)/(eL_{\text{SOL}}) \equiv [T_e(a)/e][-d \ln T_e/d\rho]_{\text{SOL}} > 0$ which would induce a small $\psi'_p \Omega_t(a) \sim T_e/(eL_{\text{SOL}}) \ll (1/n_i q_i)(-dp_i/d\rho) \equiv T_i/(eL_{p_i})$ — mainly because usually $T_i \gg T_e$ at the separatrix. In addition, in many H-mode pedestals the effects of the ion poloidal flow ($\propto c_p dT_i/d\rho$) and the many “extra” toroidal rotation effects discussed above often don’t change Ω_t much from its value on the separatrix. Thus, in pedestals the radial electric field is typically nearly equal to the ion pressure gradient: $E_\rho \simeq (1/n_i q_i)(dp_i/d\rho)$. The degree to which these two dominant terms in (45) do not cancel produces the plasma toroidal flow in the pedestal. This observation provides another interpretation of the physical processes involved in the new interpretive density transport analysis procedure²⁹ via the resultant net toroidal species rotation providing the small net thermodynamic drive for density transport in the pedestal (see Section 9 of Ref. 1).

IX. DIMENSIONLESS VARIABLE SCALINGS

The natural dimensionless variables of the paleoclassical transport model are very different from the usually used ones — see Eqs. (63) and (64) and the surrounding discussion in Ref. 7. The key parameter in the paleoclassical model is the magnetic field diffusivity D_η . It can be scaled to the reference diffusivity $\eta_0/\mu_0 = (m_e \nu_e)/(n_e e^2 \mu_0) = \nu_e \delta_e^2$. Noting from (3)–(6) that $\eta_{\parallel}^{\text{nc}}/\eta_0 = f^{\text{nc}}(Z_{\text{eff}}, \epsilon, \nu_{*e})$, in terms of the electromagnetic skin depth δ_e and the natural paleoclassical variables the key electron temperature gradient scale length prediction in (30) can be written as

$$L_{T_e} \simeq \delta_e \frac{\nu_e \delta_e (n_e T_e)}{\langle |\nabla \rho| \rangle \hat{P}_e/S} f^{\text{nc}}(Z_{\text{eff}}, \epsilon, \nu_{*e}). \quad (46)$$

This form illustrates that in this paleoclassical-based pedestal structure model the electron temperature gradient scale length in the pedestal is a multiple of δ_e .

In this paleoclassical-based model the plasma gradients and profiles within the pedestal do not depend explicitly on the usual dimensionless parameters of normalized ion gyroradius $\varrho_* \equiv \varrho_i/a$ or relative pressure $\beta \equiv P/(B^2/2\mu_0)$. The lack of a dependence on ϱ_* agrees with JET/DIII-D comparison experiments³³ which found essentially no dependence of the pedestal width or profile on ϱ_* as it was varied by a factor of four. However, the height of the pedestal is determined in this pedestal structure model by the transition from paleoclassical to electron-gyroBohm-scaling ETG-driven anomalous electron heat transport. This introduces a β_e dependence into the initial, transport-limited pedestal height. To see this note that $\chi_e^{\text{gB}} \sim [v_{T_e}/(2\sqrt{2}L_{T_e})] \varrho_e^2$ (here the electron thermal speed is $v_{T_e} \equiv \sqrt{2T_e/m_e}$ and $\varrho_e \equiv v_{T_e}/\omega_{ce}$ is the electron thermal gyroradius) whereas the paleoclassical $\chi_e^{\text{pc}} \simeq (3/2)M\nu_e \delta_e^2 \sim (v_{T_e}/\pi R_0 q) \delta_e^2$. When these different transport mechanisms are equated to determine T_e at the top of the pedestal, they naturally yield $\varrho_e^2/\delta_e^2 = \beta_e^{\text{ped}} \sim (v_{T_e}/R_0 q)/(v_{T_e}/L_{T_e}) \sim (L_{T_e}/R_0 q)$, as obtained in (35).

X. DISCUSSION

The preceding sections have developed predictions for the pedestal structure properties of the electron density profile (26), pedestal density gradient scale length (27), electron temperature gradient (30), T_e gradient scale length (31), ETG-limited height of the electron pressure pedestal (35), T_i gradient scale length (37) and lowest order plasma toroidal rotation profile (41). These predictions have been shown to be within a factor of about two or less of the properties of the DIII-D 98889 pedestal.¹ Also, as shown in Figs. 2 and 3, the magnitudes and profiles of the electron heat diffusivity, and density profiles in the pedestal have been found to approximately

agree with this model's predictions in the DIII-D 98889 pedestal⁶ and in NSTX pedestals⁵ both with and without lithium-coated walls. Further, as discussed in Section VIII the predicted effects on plasma toroidal rotation Ω_t induced by charge-exchange momentum losses and 3D field effects in the pedestal are in qualitative agreement with trends in the relevant experimental data. Thus, all aspects of this new paleoclassical-based pedestal structure model seem to be in reasonable accord with experimental results.

Maybe one should not expect better than factor of two agreement given the experimental error bars and the fact that paleoclassical theory has undetermined order unity coefficients.^{4,7} For example, as discussed in connection with quasi-symmetric stellarators in Ref. 8, the paleoclassical model D_η should be multiplied by the fraction of local FSA poloidal magnetic flux caused by parallel current flowing in the plasma. Thus, the D_η in (1) should really be multiplied by a factor $(\partial\psi_J/\partial\rho)/(\partial\psi_p/\partial\rho) \leq 1$ in which ψ_J is the poloidal magnetic flux that results from the FSA current density on that surface and ψ_p is the total poloidal flux there. Since at the separatrix X-point the plasma-current-induced poloidal magnetic field just balances that produced by the divertor coil currents, just inside the separatrix D_η might be reduced by up to a factor of two, but likely much less than that.

The pedestal height prediction in (35) can also be written in a form similar to a prediction for the normalized pedestal electron pressure gradient:

$$R_0 q \frac{\beta_e^{\text{ped}}}{L_{T_e}} \sim \frac{3\sqrt{2}}{\pi c_\#} \frac{\eta_\parallel^{\text{pc}}}{\eta_0} \frac{a^2/\bar{a}^2}{\langle |\nabla\rho|^2 \rangle} \sim 1. \quad (47)$$

This form resembles the key ideal MHD instability parameter $\alpha \equiv -R_0 q^2 d\beta/d\rho$ for high n ballooning modes⁶⁰ and for peeling-ballooning (P-B) instabilities.⁶¹ However, the derivation of (47) is based on entirely different physics (balance of paleoclassical and ETG-induced anomalous transport, rather than ideal MHD instability criteria) and its implications are entirely different.

Equations (35) or (47) plus (27) and (36) predict the initial pressure gradient a pedestal will attain in transport quasi-equilibrium. If, after an L-H transition, this is less than the P-B instability criterion⁶¹ for triggering an ELM, the pedestal evolves to this state in a time $\tau \sim (2L_{T_e})^2/\bar{D}_\eta$ ($\sim [(0.04)(0.77)]^2/[(1.6)(0.345)] \sim$ few ms for 98889 parameters). However, its top typically continues to evolve, growing and spreading inward slowly²⁸ as the core plasma heats up slowly on the global plasma energy confinement time scale ($\tau_E \sim 150$ ms in 98889).

In this pedestal structure model the n_e and T_e profiles within the pedestal (regions II and III in Fig. 1) should remain nearly invariant on time scales longer than a few ms. However, since $\chi_e^{\text{ETG}} \sim T_e^{3/2}/L_{T_e}$ whereas $\chi_{e\text{eff}}^{\text{pc}} \sim T_e^{1/2}$, the top of the pedestal should move further inward as the core electron temperature increases which reduces the T_e curvature and gradient (and hence ETG-drive) at the “top” of the pedestal. In this model

the continuing growth and inward spreading of the top of the pedestal T_e [and n_e via (26)] should eventually cause the P-B instability boundary to be exceeded and precipitate a Type I ELM. Presumably the same scenario would transpire between repetitive Type I ELMs.

If just after an L-H transition the effective conductive electron power P_e flowing through the pedestal were larger, it would require a larger T_e gradient to carry the needed electron heat flow through the pedestal. The resultant larger pedestal electron pressure gradient would probably reach the P-B instability criterion quicker and precipitate more frequent Type I ELMs. At even higher electron power flows the P-B instability boundary could be reached even faster and precipitate ELMs before the transport quasi-equilibrium discussed here could be established; in this scenario T_e should increase about linearly between ELMs. On the other hand, if the high- n ballooning limit were exceeded, particularly in the bottom half (III) of the pedestal, Type II ELMs might occur.

The alternative mechanism that is proposed⁶² to determine the pedestal structure as it evolves toward the P-B instability boundary is that the plasma pressure gradient in the edge is limited by the critical gradient for the onset of virulent high- n kinetic ballooning modes (KBMs⁶⁵). Thus, it is proposed⁶² that as the edge plasma evolves it hovers near the KBM critical gradient throughout the entire edge and pedestal region. It is possible that this “global” KBM-based pressure-gradient constraint model and the local pedestal structure model developed here are complementary — perhaps the initial pedestal structure and evolution are governed by this paper's local pedestal structure model but just before an ELM occurs KBMs further constrain the edge pressure profile.

The total pedestal pressure profile width^{63,64} is usually quoted in terms of the tanh fit parameter of it in terms of the normalized poloidal magnetic flux; for example, $\Delta_{\Psi_N} \simeq 0.076 \beta^{1/2}$ for DIII-D pedestals⁶² in which $\beta_{p,\text{ped}}$ is the poloidal β at the top of the pedestal. As noted after Eq. (31), the width of the T_e pedestal (in terms of ρ) is $\Delta_{\rho_N} \simeq 2L_{T_e}$. Thus, (47) can be used to estimate the T_e gradient width part of the total plasma pressure gradient width. While the Δ_{ρ_N} thus predicted is of order the experimentally-inferred Δ_{Ψ_N} , the scaling with plasma pressure and current are different. However, the prediction in (47) only applies to the steep gradient region of the pedestal whereas the Δ_{Ψ_N} parameter represents the tanh fit to the entire (slowly evolving) pedestal profile. Detailed measurements and analysis are needed to determine the relative roles of paleoclassical processes and KBMs in shaping the edge plasma profiles during the dynamic evolution of H-mode pedestals.

The addition of large enough anomalous electron density and heat transport in the pedestal will cause the plasma to revert to a low-confinement (L)-mode state. In this pedestal structure model this will occur when the anomalous density and heat transport flows exceed the corresponding paleoclassical flows in (16) and (20). However, the effective paleoclassical density and electron heat

diffusivities are quite different in the pedestal. The effective paleoclassical density diffusivity $D_{\text{eff}}^{\text{pc}}$ is smaller than D_η because it represents the degree to which the diffusive density flux is cancelled by the pinch flux in the paleoclassical transport model: $D_{\text{eff}}^{\text{pc}} \sim c_D D_\eta \ll D_\eta$, in which $c_D \ll 1$ ($c_D \sim D^{\text{add}}/D_\eta \lesssim 1/3$ at ρ_{mid} in 98889). However, $\chi_e^{\text{pc}} \simeq (3/2)(M+1)D_\eta$ can be much larger than D_η ($\chi_e^{\text{pc}} \simeq 4D_\eta$ at ρ_{mid} in 98889). Thus, the paleoclassical electron heat diffusivity χ_e^{pc} is typically an order of magnitude larger than the effective density diffusivity $D_{\text{eff}}^{\text{pc}} \sim c_D D_\eta$ in the pedestal.

For the most likely types of microturbulence-induced anomalous transport in the edge caused by fluid-like drift-wave modes (see for example Ref. 66 and references cited therein), the effective anomalous diffusivities for electron density and heat transport are comparable: $D^{\text{an}} \sim \chi_e^{\text{an}}$, physically because of the simultaneous advection of density and temperature by the $\tilde{\mathbf{E}} \times \mathbf{B}$ flow fluctuations.

Thus, a small amount of additional transport induced by microturbulence or some other process could modify density transport in the pedestal without significantly influencing the electron heat transport there. Specifically, if $D^{\text{an}} \gtrsim [(a^2/\bar{a}^2)/\langle |\nabla\rho|^2 \rangle] c_D D_\eta$ ($\sim 0.3 D_\eta$ at ρ_{mid} in the 98889 pedestal) but $\chi_e^{\text{an}} \ll [(a^2/\bar{a}^2)/\langle |\nabla\rho|^2 \rangle] \chi_e^{\text{pc}}$ ($\simeq 3 D_\eta$ at ρ_{mid} in the 98889 pedestal), the $n_e \bar{D}_\eta \simeq \text{constant}$ relation in (26) would no longer be valid but the $dT_e/d\rho$ prediction in (30) would still be valid in the pedestal, albeit with $dT_e/d\rho$ varying spatially there. Thus, if some small “controlled” additional pedestal density transport is added it could reduce $|dn_e/d\rho|$ but not change $dT_e/d\rho$ much and thereby possibly prevent ELMs.

This weak anomalous transport scenario provides a possible interpretation for the ELM-free EHO-induced Quiescent H- (QH-) modes in DIII-D⁶⁷ and EDA H-modes in C-Mod⁶⁸ which have low frequency quasi-coherent magnetic fluctuations in their pedestals. Also, this scenario could provide an interpretation for the I-mode regime in C-Mod^{68,69} in which the density profile had no pedestal transport barrier (i.e., if L-mode like) but the T_e profile exhibited a normal H-mode-like pedestal in the presence of weakly-coherent high frequency modes.⁶⁹ For large anomalous transport that causes $\chi_e^{\text{an}} > [(a^2/\bar{a}^2)/\langle |\nabla\rho|^2 \rangle] \chi_e^{\text{pc}}$ and $D^{\text{an}} > [(a^2/\bar{a}^2)/\langle |\nabla\rho|^2 \rangle] D_\eta$ the edge should revert to an L-mode with no n_e or T_e transport barriers or pedestals.

This pedestal structure model can also provide a qualitative interpretation for some properties of pedestals in the ELM-free state achieved by applying RMPs in DIII-D.^{56,70} A key observation of those experiments is that RMPs cause density “pumpout” — the electron density is reduced throughout the pedestal by a factor of about two⁷⁰ and the toroidal plasma rotation there increases.⁵⁶ Also, the pedestal T_e gradient about doubles but T_e on the separatrix and the T_e pedestal height remain approximately constant.⁷⁰ These RMP-induced changes can be interpreted in terms of this pedestal structure model as follows. As discussed in Section VIII, the

density pumpout in the pedestal could be produced by the extra radial electron density flux [see Eq. (113) in Ref. 16] induced by the toroidal torque $\langle \mathbf{e}_\zeta \cdot \bar{\mathbf{S}}_m \rangle > 0$ caused by a magnetic-stochasticity-induced electron direct loss current⁵⁷ $\langle \mathbf{J}_{\text{edl}} \cdot \nabla\psi_p \rangle$ in the plasma edge. Alternatively, resonant RMP components create singular layer toroidal torques in the vicinity of their rational surfaces that induce an extra radial electron density flux (see last term of Eq. (125) in Ref. 16). Both these processes also increase Ω_t in the edge region. For a pedestal with half the density, the T_e gradient should double to carry the same amount of radial electron heat flow, as (30) predicts. This causes the T_e gradient scale length L_{T_e} in (31) to decrease by a factor of two and hence the pedestal electron pressure to also decrease by this factor, as (35) predicts. These effects are qualitatively what is often observed.^{56,70} While the reduced “initial” β_e^{ped} is more likely to be below the peeling-ballooning instability boundary, the top of the pedestal could still continue to evolve and precipitate an ELM unless its evolution is halted by some other process.

XI. EXPERIMENTAL AND MODELING VALIDATION TESTS

The preceding sections have demonstrated that the H-mode pedestal structure model developed in this paper is quantitatively consistent with many properties of the DIII-D 98889 pedestal,^{1,6} and NSTX pedestals with and without lithium-coated walls.⁵ It is also qualitatively consistent with typical temporal evolution characteristics of H-mode edge plasmas and with pedestal properties in QH-modes, EDA H-modes, I-modes and RMP H-mode plasmas. However, its key scaling properties need to be explored experimentally. Also, its predictions need to be tested quantitatively against much wider data sets. Such a study using the DIII-D pedestal database has recently been completed.⁷¹ In addition, its predictions need to be tested in many other experimental devices. And finally, hopefully some of its predictions can lead to new regimes where ELMs are prevented or better controlled. All of these types of studies are needed to truly validate this model.

The paleoclassical transport model provides lower limits on radial transport of plasma density, temperatures and plasma toroidal rotation (and hence E_ρ). It is based on Coulomb collision processes that cause the plasma resistivity which produces the magnetic field diffusivity $D_\eta \equiv \eta_{\parallel}^{\text{nc}}/\mu_0$ that is so fundamental to paleoclassical transport^{3,4} and this pedestal structure model. However, like neoclassical transport theory,^{18,20} there is no underlying phenomenology that can be tested to validate the fundamental phenomenologies of the model — beyond noting that the electrical parallel resistivity in tokamak plasmas usually agrees with neoclassical predictions. Also, as noted in Section III, paleoclassical electron heat transport predictions compare favorably with exper-

imental data from many ohmic-level toroidal plasmas^{13,15} and in tokamak H-mode pedestals.^{1,5,6,13}

The pedestal structure model developed in this paper depends critically on the pedestal density profile being determined by the paleoclassical diffusive outward density flux nearly balancing its intrinsic inward pinch flux. Further interpretive transport modeling studies like those pioneered by Stacey and Groebner²⁹ are needed to identify the range of parameters over which the density pinch flux plays a critical role in determining density transport in the pedestal. Also, a direct experimental measurement of the density pinch flux would be of fundamental importance in validating that new interpretive procedure and this pedestal structure model. Finally, modeling studies using the paleoclassical diffusion and pinch fluxes in (12) could be quite helpful in clarifying the relative roles of paleoclassical density transport, neutral fueling and any needed additional density flux in the formation and evolution of H-mode pedestals; such studies are just beginning.⁷²

Validation tests can be identified for the paleoclassical-based pedestal structure model developed in this paper. A hierarchy of the most important tests are:

Fundamental Test #1: Is the T_e gradient in the pedestal approximately spatially constant and of the magnitude predicted in (30)? The constancy of $dT_e/d\rho$ depends on the constancy of $[V'\bar{D}_\eta n_e]$ and the effective conductive electron heat flow P_e through the pedestal.

Fundamental Test #2: Is $n_e(\rho)\bar{D}_\eta(\rho)$ approximately constant within the pedestal, as predicted in (26)? Exploring this is complicated by the needs for a good $Z_{\text{eff}}(\rho)$ profile and for an accurate determination of the neoclassical parallel resistivity profile.

Fundamental Test #3: Is the scaling of the electron temperature gradient scale length $[L_{T_e}/a]$ at the pedestal mid-point as predicted in (31) ?

Fundamental Test #4: Can it be shown that plasma fluctuations in the pedestal steep gradient region (II and III in Fig. 1) do not contribute dominantly to plasma transport there?

Secondary tests that are either less fundamental or result from adding information from other plasma transport models or additional sources and losses are:

Secondary Test #1: In the presence of edge neutral recycling and possible collisional- and microturbulence-induced additional density transport, is the density gradient scale length governed by (27) at the pedestal mid-point ρ_{mid} ? And do these effects cause the pedestal n_e profile to be shifted increasingly outward relative to the T_e profile as ϱ_* is decreased (via higher B_t and increased NB power, fueling, density) in DIII-D but have no significant effect on the “aligned”

profiles in JET, as observed in the JET/DIII-D comparison experiments?³³

Secondary Test #2: Does the top of the density pedestal occur where the edge T_e profile “saturates” and \bar{D}_η becomes nearly constant (e.g., $d \ln \bar{D}_\eta / d\rho \lesssim 10/a$) or is it determined by D^{an} there?

Secondary Test #3: Is the “initial” ($>$ a few ms after an L-H transition or ELM) quasi-stationary pedestal electron pressure height predicted by the β_e^{ped} in (35)? And at the top of the T_e pedestal do ETG-type fluctuations cause $\chi_e^{\text{ETG}} \gtrsim [(a^2/\bar{a}^2)/\langle |\nabla\rho|^2 \rangle] \chi_e^{\text{pc}}$ there?

Secondary Test #4: Can it be shown from predictive transport modeling of H-mode pedestals using a combination of paleoclassical and core-based anomalous transport which includes ETG-induced anomalous electron heat transport that the edge plasma evolves toward the peeling-ballooning MHD instability boundary as discussed in the fourth through sixth paragraphs in Section X? In particular, do the pedestal profiles quickly reach an invariant state and the pedestal top T_e and n_e continue to grow and spread inward?

Secondary Test #5: When charge-exchange effects on the edge plasma momentum are negligible, is the total plasma toroidal rotation frequency $\Omega_t \simeq V_t/R$ nearly constant within the pedestal at its separatrix value $\Omega_t(a)$ as predicted by (41)? When charge-exchange momentum losses are significant do they modify $\Omega_t(\rho)$ as indicated in (42)?

XII. SUMMARY

The pedestal structure model developed here assumes paleoclassical plasma transport processes dominate in a quasi-equilibrium H-mode pedestal. The T_e gradient is predicted to respond to the large radial electron heat flow through the pedestal by increasing until (30) is satisfied, which yields the T_e gradient scale length given by (31). The T_i gradient and its scale length are predicted similarly and specified in (36) and (37). Since local fueling and other density transport processes are often small compared to the characteristic level of paleoclassical radial density transport in the pedestal, the n_e profile is predicted to adjust to approximately satisfy (26). This $n_e(\rho)$ causes the net paleoclassical density transport in the pedestal to be small by nearly balancing its outward diffusive density flux with its intrinsic inward pinch flux [cf., Eq. (12)]. It also causes approximate “alignment” of the n_e and T_e profiles in the pedestal. When edge fueling (or additional density transport) is significant it can increase (decrease) the predicted $|dn_e/d\rho|$ in the pedestal, as indicated in (27). The

initial, transport-limited height of the pedestal is predicted from a posited transition from paleoclassical electron heat transport in the pedestal (region II) to ETG-induced electron-gyroBohm-scaling anomalous transport in the core (region I) plasma, as given by (35) and (47).

When toroidal momentum sources and losses in the pedestal are small compared to paleoclassical toroidal momentum transport processes, the total plasma toroidal rotation Ω_t is predicted in (41) to be nearly constant in the pedestal, at its value on the separatrix. When charge-exchange-induced plasma momentum losses are significant, they are predicted to cause $d\Omega_t/d\rho > 0$ in the pedestal, as indicated in (43). The effects of 3D fields can also modify Ω_t (see Section VIII). The radial electric field in the pedestal is determined by substituting the thus determined Ω_t into the radial force balance, as indicated in (45).

All these pedestal structure predictions have been shown to agree within a factor of about two or less with data from the low collisionality DIII-D 98889 pedestal.^{1,6} Also, as shown in Figs. 2 and 3, the χ_e magnitudes and profiles, and n_e profiles in the DIII-D 98889 pedestal⁶ and NSTX H-mode pedestals with and without lithium wall coatings⁵ are captured by this model. The predicted pedestal structure does not depend on ϱ_* ; this agrees with results from recent JET/DIII-D comparison experiments.³³ This model also provides a framework for interpreting pedestal structure properties in DIII-D QH-modes,⁶⁷ C-Mod EDA H-modes⁶⁸ and I-modes^{68,69} — as being due to pedestal n_e profile changes caused by additional density transport with electron heat transport at the same level having a minimal effect on the pedestal T_e profile. Also, the model provides qualitative interpretations for some of the effects of RMPs on H-mode pedestals observed in DIII-D:^{56,70} density pumpout (via stochasticity-induced direct electron losses⁵⁷ or resonant layer effects), but T_e gradient and Ω_t increases, the same T_e^{ped} , and L_{T_e} and β_e^{ped} reductions in the pedestal steep gradient region (II, III in Fig. 1).

Finally, the model predicts long period Type I ELMs like those in Refs. 1, 28 occur when the radial electron power flow through the pedestal is small enough so the transport quasi-equilibrium T_e gradient predicted by this model can be reached without triggering ideal MHD peeling-ballooning instabilities.⁶¹ Then, after a pedestal equilibration time (\sim few ms in 98889) the pedestal structure in the steep gradient region (II and III in Fig. 1) is predicted to remain roughly invariant. However, the top of the pedestal increases and moves inward on a longer time scale. It usually eventually exceeds the peeling-ballooning instability boundary and precipitates an ELM. At higher power levels the ELMs are likely to become more frequent. If the transport quasi-equilibrium discussed here cannot be established before a Type I ELM occurs, T_e^{ped} would increase nearly linearly between ELMs. Or perhaps Type II ELMs would be triggered by high- n ballooning modes in the bottom half (region III) of the pedestal before a Type I ELM occurs.

The preceding section suggests a hierarchy of experimental and modeling tests to validate this pedestal structure model. It also discusses some possible avenues that emerge from this new model for reducing the pedestal electron pressure gradient or height and perhaps thereby avoiding, controlling or delaying the onset of ELMs.

ACKNOWLEDGMENTS

The author is very grateful to R.J. Groebner for his patient and constructive discussions over the past few years about the many physics issues and experimental measurements involved in understanding pedestal plasma transport. He is also grateful to T.H. Osborne who developed and with R.J. Groebner made accessible and extended where necessary the outstanding 98889 DIII-D pedestal data set upon which much of this analysis is based. The continuing collaboration of his colleagues in the H-Mode Edge Pedestal (HEP) Benchmarking Exercise (BE) that resulted in Ref. 1 is also greatly appreciated.

The author would also like to emphasize the importance of the pioneering pedestal transport analysis studies by W.M. Stacey and R.J. Groebner (see Refs. 29, 52 and references cited therein) which used experimental information on ion flows to infer density pinch flows in pedestals. Those studies provided a key impetus for the density transport analysis that leads to (26).

Finally, the author is grateful to J.M. Canik, A.Y. Pankin and S.P. Smith for their implementation and initial tests of various aspects of this pedestal structure model. In particular, the NSTX tests⁵ highlighted the need to carefully account for the strong f_t/f_c effects in D_η formulas at low aspect ratio ($f_t/f_c \sim 13$ in NSTX pedestals). Initial predictive transport modeling studies⁷² of pedestal density profiles have been helpful in illuminating some density pinch flux issues. Finally, initiation of tests⁷¹ of many model predictions against the DIII-D pedestal database has helped clarify many detailed aspects of the model. These studies have all helped improve and focus the model since it was originally presented in an unpublished report UW-CPTC 10-6, August 30, 2010.

This research was supported by U.S. Department of Energy grant DE-FG02-92ER54139.

REFERENCES

- ¹J.D. Callen, R.J. Groebner, T.H. Osborne, J.M. Canik, L.W. Owen, A.Y. Pankin, T. Rafiq, T.D. Rognlien and W.M. Stacey, Nucl. Fusion **50**, 064004 (2010).
- ²J. Luxon, Nucl. Fusion **42**, 614 (2002).
- ³J.D. Callen, Phys. Rev. Lett. **94**, 055002 (2005). See <http://homepages.cae.wisc.edu/~callen/paleo> for an annotated list of paleoclassical model publications, including those that provide derivations of its key hypothesis. References 3–13 and 15–17

- are available or accessible via this same webpage or <http://www.cae.wisc.edu/~callen/tokamaks>.
- ⁴J.D. Callen, Phys. Plasmas **12**, 092512 (2005).
 - ⁵J.M. Canik et al., Phys. Plasmas **18**, 056118 (2011).
 - ⁶J.D. Callen, J.M. Canik and S.P. Smith, "Pedestal Structure Model," submitted to Phys. Rev. Lett., (UW-CPTC 11-3, July 2011, available from <http://www.cptc.wisc.edu>.)
 - ⁷J.D. Callen, Nucl. Fusion **45**, 1120 (2005).
 - ⁸J.D. Callen, Phys. Plasmas **14**, 040701 (2007).
 - ⁹L.L. LoDestro, Phys. Plasmas **14**, 104701 (2007).
 - ¹⁰J.D. Callen, Phys. Plasmas **14**, 104702 (2007).
 - ¹¹J.W. Connor, R.J. Hastie and J.B. Taylor, Phys. Plasmas **15**, 014701 (2008).
 - ¹²J.D. Callen, Phys. Plasmas **15**, 014702 (2008).
 - ¹³J.D. Callen, J.K. Anderson, T.C. Arlen, G. Bateman, R.V. Budny, T. Fujita, C.M. Greenfield, M. Greenwald, R.J. Groebner, D.N. Hill, G.M.D. Hogeweij, S.M. Kaye, A.H. Kritiz, E.A. Lazarus, A.C. Leonard, M.A. Mahdavi, H.S. McLean, T.H. Osborne, A.Y. Pankin, C.C. Petty, J.S. Sarff, H.E. St. John, W.M. Stacey, D. Stutman, E.J. Synakowski and K. Tritz, Nucl. Fusion **47**, 1449 (2007).
 - ¹⁴R. Aymar, V.A. Chuyanov, M. Huguet, Y. Shimomura and ITER Joint Central Team and ITER Home Teams, Nucl. Fusion **41**, 1301 (2001).
 - ¹⁵G.M.D. Hogeweij, J.D. Callen, RTP team and TEXTOR team, Plasma Phys. Control. Fusion **50**, 065011 (2008).
 - ¹⁶J.D. Callen, A.J. Cole, and C.C. Hegna, Phys. Plasmas **16**, 082504 (2009).
 - ¹⁷J.D. Callen, C.C. Hegna, and A.J. Cole, Phys. Plasmas **17**, 056113 (2010).
 - ¹⁸F.L. Hinton and R.D. Hazeltine, Rev. Mod. Phys. **48**, 239 (1976).
 - ¹⁹S.P. Hirshman, R.J. Hawryluk and B. Birge, Nucl. Fusion **17**, 611 (1977).
 - ²⁰S.P. Hirshman and D.J. Sigmar, Nucl. Fusion **21**, 1079 (1981).
 - ²¹O. Sauter, C. Angioni and Y.R. Lin-Liu, Phys. Plasmas **6**, 2834 (1999).
 - ²²See UW-CPTC 09-6R available as supplementary material for Reference [11] in Reference 17 via <http://ftp.aip.org/epaps/phys.plasmas/E-PHPAEN-17-033091/033091php.pdf> or as UW-CPTC_09-6.rev at <http://www.cptc.wisc.edu>.
 - ²³W.A. Houlberg, K.C. Shaing, S.P. Hirshman and M.C. Zarnstorff, Phys. Plasmas **4**, 3230 (1997).
 - ²⁴Y.B. Kim, P.H. Diamond and R.J. Groebner, Phys. Fluids B **3**, 2050 (1991); Erratum, Phys. Fluids B **4**, 2996 (1992).
 - ²⁵See supplementary material at [URL to be supplied by AIP] for ParNeoRes.pdf file for evaluating the parallel neoclassical resistivity. Also available as UW-CPTC 11-5, July 2011 via <http://www.cptc.wisc.edu>.
 - ²⁶C.T. Hsu, K.C. Shaing, R.P. Gormley and D.J. Sigmar, Phys. Fluids B **4**, 4023 (1992).
 - ²⁷Y.R. Lin-Liu and R.L. Miller, Phys. Plasmas **2**, 1666 (1995).
 - ²⁸R.J. Groebner, T.H. Osborne, A.W. Leonard and M.E. Fenstermacher, Nucl. Fusion **49**, 045013 (2009).
 - ²⁹W.M. Stacey and R.J. Groebner, Phys. Plasmas **16**, 102504 (2009).
 - ³⁰R.J. Groebner et al., Phys. Plasmas **9**, 2134 (2002).
 - ³¹M.A. Mahdavi et al., Phys. Plasmas **10**, 3984 (2003).
 - ³²J.W. Hughes et al., Phys. Plasmas **13**, 056103 (2006).
 - ³³M.N.A. Beurskens, T.H. Osborne et al., Plasma Phys. Control. Fusion **51**, 124051 (2009).
 - ³⁴W. Horton, B. Hong and W.M. Tang, Phys. Fluids **31**, 2971 (1988).
 - ³⁵F. Jenko, W. Dorland and G.W. Hammett, Phys. Plasmas **8**, 4096 (2001).
 - ³⁶F. Jenko, D. Told, P. Xanthopoulos, F. Merz and L.D. Horton, Phys. Plasmas **16**, 055901 (2009).
 - ³⁷D.P. Coster et al., in *Fusion Energy 2008* (Proc. 22nd Int. Conf. Geneva, 2008) (Vienna: IAEA) CD-ROM file TH/P4-3 and <http://www-naweb.iaea.org/napc/physics/FEC/FEC2008/html/index.htm>.
 - ³⁸W. Suttrop et al., Plasma Phys. Control. Fusion **39**, 2051 (1997).
 - ³⁹G. Saibene et al., Nucl. Fusion **39**, 1133 (1999).
 - ⁴⁰T.H. Osborne et al., Plasma Phys. Control. Fusion **42**, A175 (2000).
 - ⁴¹A.E. Hubbard et al., Phys. Plasmas **14**, 056109 (2007).
 - ⁴²H. Urano et al., Nucl. Fusion **49**, 095006 (2009).
 - ⁴³J. Kim et al., Phys. Rev. Lett. **72**, 2199 (1994).
 - ⁴⁴P. Monier-Garbet et al., Nucl. Fusion **37**, 403 (1997).
 - ⁴⁵K.D. Marr et al. Plasma Phys. Control. Fusion **52**, 055010 (2010).
 - ⁴⁶G. Kagan and P.J. Catto, Plasma Phys. Control. Fusion **52**, 055004 (2010).
 - ⁴⁷A.R. Field et al., Plasma Phys. Control. Fusion **51**, 105002 (2009).
 - ⁴⁸R.E. Bell et al., Phys. Plasmas **17**, 082506 (2010).
 - ⁴⁹K.H. Burrell et al., Bull. Am. Phys. Soc. **55** (No. 15), 131 (2010) (to be published).
 - ⁵⁰J.D. Callen, A.J. Cole and C.C. Hegna, Nucl. Fusion **49**, 085021 (2009).
 - ⁵¹J.D. Callen, Nucl. Fusion **51**, 094026 (2011).
 - ⁵²W.M. Stacey, Phys. Plasmas **17**, 052506 (2010).
 - ⁵³J.S. deGrassie et al., Phys. Plasmas **14**, 056115 (2007).
 - ⁵⁴T. Pütterich et al., Phys. Rev. Lett. **102**, 025001 (2009).
 - ⁵⁵F.L. Hinton and M.N. Rosenbluth, Phys. Lett. A **259**, 267 (1999).
 - ⁵⁶T.E. Evans et al., Nucl. Fusion **48**, 024002 (2008).
 - ⁵⁷S. Mordijck et al., Plasma Phys. Control. Fusion **53**, 122001 (2011).
 - ⁵⁸A.M. Garofalo et al., Phys. Rev. Lett. **101**, 195005 (2008).
 - ⁵⁹A.M. Garofalo et al., Phys. Plasmas **16**, 056119 (2009).
 - ⁶⁰J.W. Connor, R.J. Hastie and J.B. Taylor, Phys. Rev. Lett. **40**, 396 (1978).
 - ⁶¹P.B. Snyder et al., Phys. Plasmas **9**, 2037 (2002).
 - ⁶²P.B. Snyder, R.J. Groebner, A.W. Leonard, T.H. Os-

- borne and H.R. Wilson, *Phys. Plasmas* **16**, 056118 (2009).
- ⁶³R. J. Groebner and T. H. Osborne, *Phys. Plasmas* **5**, 1800 (1998).
- ⁶⁴T.H. Osborne, K.H. Burrell, R.J. Groebner, L.L. Lao, A.W. Leonard, R. Maingi, R.L. Miller, G.D. Porter, and A.D. Turnbull, *J. Nucl. Mater.* **266269**, 131 (1999).
- ⁶⁵P.B. Snyder and G.W. Hammett, *Phys. Plasmas* **8**, 744 (2001).
- ⁶⁶T. Rafiq, G. Bateman, A.H. Kritz and A.Y. Pankin, *Phys. Plasmas* **17**, 082511 (2010).
- ⁶⁷K.H. Burrell et al., *Phys. Plasmas* **12**, 056121 (2005).
- ⁶⁸R. M. McDermott et al., *Phys. Plasmas* **16**, 056103 (2009).
- ⁶⁹D.G. Whyte et al., *Nucl. Fusion* **50**, 105005 (2010).
- ⁷⁰T.E. Evans et al., *Nature Physics* **2**, 419 (2006).
- ⁷¹S.P. Smith, J.D. Callen, R.J. Groebner, T.H. Osborne, A.W. Leonard, D. Eldon, B.D. Bray and the DIII-D Team, "Comparing paleoclassical based model predictions of electron quantities to measured DIII-D H-mode profiles," P3.1 at H-mode Workshop, Oxford, UK, 10-12 October 2011 (to be submitted to *Nuclear Fusion*).
- ⁷²A. Pankin et al., "Study of H-mode Pedestal Buildup Dynamics Using the FACETS Code," P5.4 at H-mode wkshp, 10-12 October 2011, Oxford, UK (to be submitted to *Nuclear Fusion*).